TAFFY PULL AND ASSOCIATES: REVIEW AND NEW OBSERVATIONS OF NORTHWESTERN HELLAS PLANITIA

H. Bernhardt, D. Reiss, M. Ivanov, E. Hauber, H. Hiesinger, J. D. Clark, R. Orosei

Abstract

Northwestern Hellas Planitia hosts landforms that are unique on Mars, e.g., the so called honeycomb and banded (aka "taffy pull") terrains. Recently, robust formation models for the ~6 km large honeycomb depressions involving salt or ice diapirism have been formulated. However, the nature of the banded terrain, a ~30,000 km² area characterized by a dm- to km-scale pattern of curvilinear troughs, has remained elusive. While previous interpretations range from deep-seated, honeycomb-related outcrops to a younger veneer, recent reports of putative periglacial features (e.g., potential thermokarst) strongly indicate it to be a relatively thin, volatile-related surface unit. In order to further constrain the origin and nature of the banded terrain, we investigated the northwestern Hellas basin floor employing various datasets. Although neither CRISM nor MARSIS/SHARAD revealed any clear signatures on and beneath the area, we used a purpose-built CTX mosaic to produce a 1:175,000 morphologic map to comprehensively characterize the banded terrain in great detail. We mapped the banded terrain's extent at high precision, showing that it partially superposes the honeycomb terrain, likely resulting in certain superposition features, but also occurs up to ~240 km away from it. Via stratigraphic analyses and crater size-frequency measurements, we bracketed the age of the banded terrain between ~2.2 and ~3.3 Ga. Furthermore, the banded terrain can be differentiated into two types, ridged and creviced, with the former predominantly occurring among the lowest

reaches of the terrain's ~2 km topographic extent. We also produced a grid map (2x2 km box size) of the entire banded terrain in order to assess the relation between band shape and local topography. As we identified no large-scale (> 25 km) band pattern and no correlation between local slope and band orientation, regional tectonics or gravity-driven flow down modern topography are unlikely to have played decisive roles for banded terrain formation. Instead, we observed numerous locations, where band slabs appear to have broken off and subsequently rotated, as well as "cusps" that seem to have resulted from buckling. Based on this, we suggest that the banded terrain experienced both, ductile deformation as well as brittle failure on or near the surface. Following this assessment, we investigated formation scenarios involving low viscosity materials, namely salt, lava, and ice/ice-rich/wet layers based on terrestrial analogy. Despite certain similarities, neither salt (as salt glaciers), lava sheets, nor land-based glaciers are in agreement with the extensive curvilinear texture and topographic/geologic setting of the banded terrain. Ice shelf margins, on the other hand, can produce surface textures akin to the banded terrain in both form and scale, even including cusps and broken off, rotated blocks. However, an ice-covered sea between 2.2 and 3.3 Ga ago is not supported by the geologic inventory of the Hellas basin, which previous investigations found to lack any landforms indicative of a standing body of water. Instead, we identified several sinuous ridges terminating at plains covered by smaller, braiding ridges, which we interpret as eskers and glacial sandurs, respectively. As both are embayed and partially covered by the banded terrain, we tentatively propose an alternative model of the banded terrain having formed as wet till that was viscously deformed according to the stress fields created by the ice overburden pressure in conjunction with bed topography. Although this formation model remains inconclusive, it is in agreement with climate models suggesting obliquity excursions and a denser, early Amazonian atmosphere to have caused ice accumulation in the adjacent northwestern Hellas basin rim, thus potentially enabling flow onto the floor entailing subglacial banded terrain formation.

1. Introduction

The northwestern Hellas basin floor on Mars hosts a highly complex landscape containing several unique landforms in close geographic association, e.g., the "honeycomb" and "banded" (or "taffy pull") terrains (e.g., *Diot et al., 2015a; Bernhardt et al., 2016a; Voelker at al., 2017*). Both of these terrains have been subject to a wide range of conflicting interpretations with profoundly different implications (*Moore and Wilhelms, 2001, 2007; Mangold and Allemand, 2003; Kite et al., 2009; Diot et al., 2015a,b; Bernhardt et al., 2016b*). One detriment for investigations is the physiographic setting of the area within Mars' largest and deepest topographically well-defined impact basin (e.g., *Andrews-Hanna and Zuber, 2010*), resulting in remote sensing observations often being compromised by atmospheric opacity and a high surface dust abundance amongst others (*Ruff and Christensen, 2002; Basu et al., 2004*). This caused previous studies of the western Hellas basin floor to focus exclusively on specific landform types and/or to rely on comprehensive low-resolution datasets and only selective high-resolution observations (e.g., *Moore and Wilhelms, 2007; Diot et al., 2015a,b; Bernhardt et al., 2016a,b; Voelker et al., 2017*). Nevertheless, these studies yielded crucial insights and concluded the honeycomb terrain to be the surface expression of diapirs, possibly of salt or ice (*Bernhardt et al., 2016b; Weiss and Head, 2017*), and the banded terrain to be some form of volatile-rich veneer (*Diot et al., 2014, 2015a*). However, profound ambiguities remain that greatly limit our understanding of these enigmatic landforms, their role in the history of water in the Hellas region, and the resulting implications for the climatic evolution of Mars.

By assembling a comprehensive, high-resolution morphologic map (on a purpose-built, seamless Context Camera mosaic), as well as a fine-scale grid mapping and further analyses based on all available datasets (including radar and hyperspectral), this investigation provides a refined assessment of northwestern Hellas Planitia with the aim of shedding more light on its enigmatic landforms.

2. Physiographic and geologic setting

The study area covers an ~670 x ~445 km large portion of northwestern Hellas Planitia (Fig. 1A), the floor of the deepest and largest (~1700 x ~1300 km) topographically well-defined impact basin on Mars (e.g., *Wood and Head, 1976; Andrews-Hanna and Zuber, 2010*). The study area was defined to encompass the honeycomb and banded terrains as mapped by *Bernhardt et al. (2016b)*, who also provided detailed descriptions of the basin's general physiography and geology. To the north, the study area reaches into central Peneus Palus, a wrinkle-ridged plain hosting the deepest area of the Hellas basin containing the lowest point on Mars at -8204 m (within Badwater crater ~65 m northeast of the study area's extent) (*Bernhardt et al., 2016a*). Displaying a high kilometer-scale roughness, Peneus Palus is partially covered by prominent ejecta, e.g., around Kufstein crater, but also by weakly consolidated materials similar to those of the hummocky basin center (*Bernhardt et al., 2016a*). Peneus Palus lies at an average elevation of ~ -7,500 m and forms the northern half of an annular, ~1,500 km long, and up to ~330 km wide depression along the western Hellas basin floor outline previously called "Hellas Planitia trough" (HPT; *Howard et al., 2012*). The western edge of the study area roughly follows the HPT, whose average elevation rises to ~ -6,800 m in its southern half, where its floor is characterized by a high 1 – 10 kilometer-scale roughness. The center portion of the floor of the HPT is dissected by a basin rim-parallel chain of ~20 – 77 km long, ~11 – 33 km wide, and up to ~200 m deep, irregularly-shaped depressions. To the east, the HPT is bound by a ~600 – ~1,000 m high scarp leading up to a central, hummocky portion of the basin previously referred to as "Alpheus Colles plateau" (*Moore and Wilhelms, 2001*). The study area encompasses the westernmost reaches of this more elevated, hummocky region, which is characterized by a high, 10 – 20 kilometer-scale roughness and includes Beloha crater (Ø ~27 km) as well as a nameless, highly degraded crater (Ø ~90 km) ~160 km southwest of it.

3. State of research

Banded terrain: After the Mars Orbiter Near Angle Camera (MOC-NA) first revealed the texture of the banded terrain, it was interpreted as sediment layers that were viscously deformed by icebergs floating on a receding Hellas sea, thereby leaving behind the honeycombs as imprints (*Moore and Wilhelms, 2001*). Later investigations maintained a genetic link between the banded and honeycomb terrains, but interpreted the observed textures to suggest multiple overturns caused by convective processes, e.g., diapirism (*Mangold and Allemand, 2003; Kite et al., 2009*). Despite the banded terrain's textural similarity to halokinetic sequences (layers viscously deformed by salt tectonics; e.g., *Jackson et al., 1990; Wilson et al., 2010; Bernhardt et al., 2016b*), batholithic diapirism (*Mangold and Allemand., 2003*) and impact melt convection (*Kite et al., 2009*) were tentatively favored over salt diapirism as formation scenarios for the honeycomb-banded terrain assemblage.

After *Thomas et al. (2010)* first differentiated between the honeycomb and banded terrains, *Diot et al. (2013)*, outlined the banded terrain's approximate extent and noted that, despite a close geographic association, its textures can occur separately from the honeycomb depressions. This crucial observation was followed by several investigations suggesting the banded terrain to be a relatively thin, volatile-rich surface layer that is unlikely to be genetically related to the honeycomb terrain (*Diot et al., 2014, 2015a,b). Diot et al. (2014)* modelled the banded terrain's crater retention age to be ~3 Ga and made several important observations, noting the presence of thermokarst-like depressions, patterned ground, pit chains, pingo-like fractured mounds, as well as individual "bands" transitioning into textures similar to other martian landforms likely resulting from periglacial processes, e.g., the brain terrain (*Levy et al., 2009*). It was also inferred that, in an ice-flow scenario, the banded terrain's average slopes of ~6° and band depths, i.e., assumed thickness, of ~12 to ~30 m could produce basal stresses of up to ~28 kPa (*Diot et al., 2014*). As this is close to the minimum value of ~30 kPa calculated for martian

lobate debris aprons/viscous flow features (VFF; *Mangold and Allemand, 2001*), a formation involving downslope creep was deemed conceivable (*Diot et al., 2014*). Furthermore, *Diot et al. (2015a)* suggested that the orientation and geometry of some selected bands appear to be a result of viscous flow across the surface, although this assessment was not based on a comprehensive, statistical analysis. Likening them to glacial crevasses, several locations were pointed out, where the bands are perpendicular to the local slope, often forming tongue-like arrangements with notable deviations mostly occurring where there are interferences between adjacent bands (*Diot et al., 2015a*). Additionally, *Bernhardt et al. (2016b)* observed apparent "slabs" detaching from a banded terrain zone of turbulent texture as well as band-perpendicular, meter-scale furrows that are much more reminiscent of glacial crevasses than the actual bands themselves and visible on almost all high-resolution images of the banded terrain. It was also pointed out that the small-scale morphology of the banded terrain (smooth surface dissected by curvilinear, crevice-like troughs) is different from that of halokinetic sequences sometimes found around terrestrial salt diapirs. While halokinetic, curvilinear patterns are reminiscent of the banded terrain, they are, in fact the result of ridges formed by steeply dipping layers of different erosion resistances and not crevice-like troughs (*Jackson et al., 1990; Bernhardt et al., 2016b*).

Honeycomb terrain: The honeycomb terrain was first identified as "reticulate floor unit" and interpreted as differentially eroded Amazonian mantle material, possibly of eolian origin (*Greeley and Guest, 1987*). A tentative eolian interpretation, albeit as compound crescentic dunes, was maintained (*Tanaka and Leonard, 1995; Leonard and Tanaka, 2001*) until high resolution MOC-NA images revealed the honeycombs' and banded terrain's details, leading to both landforms being interpreted as a single unit that is the result of wet, viscous sediments having been imprinted by icebergs floating on a receding Hellas sea (*Moore and Wilhelms, 2001, 2007*). Later, observations of highly convoluted textures (wavelengths 10s of meters) within the banded terrain motivated an interpretation of the honeycombs as upwelling

structures, either due to "lower crust vertical tectonism", i.e., batholitic diapirism (*Mangold and Allemand, 2003*), or impact melt convection (*Kite et al., 2009*). Although similarities to terrestrial salt provinces were noted, salt diapirism was not favored as formation model due to the large amount of required salt (*Kite et al., 2009*) and the lack of brittle deformation structures (*Mangold and Allemand, 2003*). However, it was later found that neither of these arguments prevent a salt scenario and that diapirism by salt, or alternatively ice, appears to be more likely than the alternative models, which face certain plausibility issues and/or whose analogs in nature, if existent at all, bear little similarities to the honeycombs (*Diot et al., 2015b; Bernhardt et al., 2016b*). Mostly depending on the weight of overburden, physical models of diapirism suggest that the spacing, size, and extent of the honeycombs would have required either ~22,000 to 130,000 km^3 of salt, or ~3,600 to 112,000 km^3 of ice (*Bernhardt et al., 2016b; Weiss and Head, 2017*). As the adjacent wrinkle ridged plains were found to partially superpose it, a Noachian age (>3.8 Ga) is implied for the honeycomb terrain, whose very low crater density was interpreted as a result of relatively recent excavation, likely by deflation (*Bernhardt et al., 2016b*). The morphometry and potential volume of the honeycomb terrain was found to be similar to terrestrial salt provinces, e.g., the Great Kavir in Iran or the Gulf of Mexico (*Bernhardt et al., 2016b*), and numerous channels leading into the Hellas basin might have supplied potentially salty water from the adjacent, chloride-bearing highlands (*Osterloo et al., 2008, 2010*; *Bernhardt et al., 2016a*). This underlines the viability of a salt diapirism scenario, thus implying climatic conditions during honeycomb formation in the Noachian that permitted at least episodic surface water runoff as well as subsequent evaporation and/or freezing/sublimation over extended time periods accumulating to no less than 3.5 m global equivalence layer (GEL) of salt-saturated water (*Bernhardt et al., 2016b*). *Weiss and Head (2017)* on the other hand emphasized the more modest prerequisites of an ice diapirism scenario, which would require no liquid water and only ~0.05 to ~0.5 m GEL worth of ice. Furthermore, preliminary model results indicate that in a denser atmosphere and with higher

obliquities (e.g., 600 mbar CO_2 and 45°), ice could have accumulated around the Hellas basin and subsequently flowed onto its floor before being buried by later deposits (*Fastook et al., 2017*). At this point, both salt as well as ice diapirism remain viable formation mechanisms for the honeycomb terrain, albeit with drastically different climatic implications.

Other landforms: The first Viking-based map covering the area characterized northwestern Hellas Planitia as transition zone between the higher-standing deposits in the basin interior and a smoother peripheral zone, now identified as HPT (*Peterson, 1977*). Due to the relatively small volume of material eroded from the then known channels leading into the Hellas basin and the apparent friability of the interior deposits, later investigations interpreted them as well as the HPT floor as different erosional states of mainly eolian materials superposing wrinkle-ridged lava plains (*Greeley and Guest, 1987; Tanaka and Leonard, 1995; Leonard and Tanaka, 2001*). Contrasting this, a mainly glacial origin of many landforms in our study area was emphasized by *Kargel and Strom (1992)*. They proposed a Noachian glacier entering the Hellas basin from the south, interpreted several wrinkle ridges as well as elongate erosional remnants in the HPT as terminal moraines, and knobs within the interior deposits as drumlins. In order to explain the honeycomb terrain as iceberg imprints, *Moore and Wilhelms (2001, 2007)* then suggested a large-scale glacio-fluvial scenario, in which an ice-covered sea filled the Hellas basin up to ~ -3,100 m. The interior deposits (called "Alpheus Colles plateau") were proposed to be sediments of that sea, whereas 100s of meters to few kilometers wide and up to ~100 km long, sinuous ridges perpendicular to the scarp delimiting the interior deposits to the southwest were tentatively interpreted as eskers laid down by meltwater beneath an ice-rich overburden after the Hellas sea had completely frozen *(Moore and Wilhelms; 2001, 2007).* However, comprehensive studies of the Hellas basin floor based on post-Viking datasets showed the morphometries and detailed morphologies of the honeycombs, as well as the afore mentioned wrinkle ridges and knobs to be unsuited for their respective glacial interpretations (*Wilson et al., 2010; Diot et al., 2015a; Bernhardt et al., 2016a*). Instead, *Greeley and Guest's*

202 *(1987)* initial interpretation of the plains north of the honeycombs as tectonically modified (i.e.,
203 wrinkle-ridged) volcanic deposits was largely affirmed, albeit with a Noachian model age (~3.8
204 Ga) and variable overlay by remnants of the hummocky interior deposits, for which a Hesperian
205 model age (~3.7 Ga) was derived (*Bernhardt et al., 2016a*). Hesperia as well as Malea Plana
206 east and south of Hellas Planitia were identified as potential sources of the estimated ~10^6 km³
207 of initial Hellas interior deposits, as similarly-aged erosional landforms there suggest the
208 removal and transport of that volume down to the basin, likely triggered by large-scale volcano-
209 ice interactions (*Ivanov et al., 2005; Bernhardt et al., 2016a; Cassanelli and Head, 2016*).
210 However, no clear morphological or textural indications for a past body of water or ice filling
211 the Hellas basin, e.g., wide-scale layering or unambiguous shoreline-like terraces, have been
212 found (*Bernhardt et al., 2016a*).

213 # 4. Data and techniques

214 The centerpiece of our investigation is a 1:175,000 morphologic map (Fig. 2A)
215 encompassing an area of 159,856 km² between 50°E 33.4°S and 61.3°E 44.3°S on the
216 northwestern Hellas basin floor. The mapping process was carried out on a purpose-built,
217 seamless Context Camera (CTX; e.g., *Malin et al., 2007*) mosaic (Fig. 1B). For this mosaic,
218 177 CTX images (~6 m/px) were co-registered and seamlessly stitched using Photoshop, after
219 which we applied a high-pass filter at the average CTX swath width to reduce brightness
220 variations along the individual image margins. For better manageability in ArcMap regarding
221 the mosaic's large size, we reduced its resolution by 50% (i.e., to ~12 m/px) and then
222 geographically aligned it to version 12 of the THEMIS-IR Day Global Mosaic (*Edwards et al.,*
223 *2011*). Stereo CTX pairs were also used to create digital elevation models (DEMs) via the Ames
224 Stereo Pipeline (e.g., *Moratto et al., 2010*) for local topographic analyses alongside the global
225 DEM by the Mars Orbiter Laser Altimeter (MOLA; *Smith et al., 2001*). Local-scale
226 observations including multi-temporal investigations were made using images by the High-

227 Resolution Imaging Science Experiment (HiRISE; 25–50 cm/px; *McEwen et al., 2007*) as well
228 as the Mars Orbiter Near-Angle Camera (MOC-NA; 1.4 to ~3 m/px; *Malin and Edgett, 2010*).
229 Within this context, our investigation was greatly enhanced by the multi-temporal database of
230 planetary image data (MUTED; *Heyer at al., 2017*), which provided swift access to zoom- and
231 scrollable, full-resolution MOC-NA as well as HiRISE data including highlighted areas of
232 overlap within and beyond the designated mapping area. In order to assess the correlation
233 between the banded terrain's texture and the local slope, we also performed a CTX mosaic-
234 based grid mapping covering its entire extent (Fig. 3). At a grid box size of 2x2 km, the banded
235 terrain encompasses 9920 boxes, each of which was assigned to one of ten categories according
236 to the general type ("creviced" or "ridged") as well as five dominant orientations of the
237 contained bands (Fig. 4): slope-perpendicular, slope-parallel, circular, lobate, and random. Also
238 using our CTX mosaic, we conducted crater size-frequency distribution (CSFD) measurements
239 on one of our morphologic units to derive an absolute model age via CraterStats (*Michael and*
240 *Neukum, 2010*).

241 We supplemented our visual and morphologic analyses with nine full- as well as three half-
242 resolution targeted (FRT and HRL/HRS) observations by the Compact Reconnaissance
243 Imaging Spectrometer for Mars (CRISM; *Murchie et al., 2007*). Using the CRISM Analysis
244 Toolkit (CAT) version 7.3.1 for ENVI to apply photometric and atmospheric corrections
245 (empirically determined "volcano scans"; *McGuire et al., 2009*), we also employed revised
246 spectral parameters by *Viviano-Beck et al. (2014)* to identify potential regions of interest whose
247 spectra were then "ratioed", i.e., divided by a nearby "spectrally bland" area, to reduce
248 ubiquitous atmospheric effects.

249 In addition to our photogeological studies, we investigated the subsurface of the Hellas
250 basin, e.g., to test diapiric (salt or ice) formation models for the honeycomb terrain. We
251 analyzed radargrams of ground penetrating radar (GPR) tracks traversing our study area, five
252 by the Mars Advanced Radar for Subsurface and Ionospheric Sounding (MARSIS; *Picardi et*

253 *al., 2004; Orosei et al., 2015*) as well as three by the Mars Shallow Radar Sounder (SHARAD;
254 *Seu et al., 2007*). We combined observations by both GPRs in order to exploit MARSIS'
255 superior penetration depth (>3.7 km in ice-rich material) as well as SHARAD's finer horizontal
256 and vertical resolutions (0.3-1 km and ~15 m) (*Seu et al., 2007*). Measured and simulated
257 radargrams by MARSIS were generated using the algorithm by *Nouvel et al. (2004)*
258 implemented as described in *Cantini et al. (2014)*. Those of SHARAD were generated using
259 the Colorado Shallow Radar Processing System (Co-SHARPS) by the Planetary Science
260 Institute (*Putzig et al., 2016*). Each radargram was correlated with its simulated counterpart to
261 prevent "clutter", i.e., echoes from surface reflections, being mistaken for signals by potential
262 subsurface reflectors.

263 # 5. Descriptions and interpretations of morphologic units

264 In this section we briefly describe all units of our morphologic map (in order of their
265 stratigraphic positions) and offer interpretations for each unit group as shown in Fig. 2B. All
266 mapped units, along with their type locality coordinates and areal extents, are listed in Table 1.
267 Standardized pictures of each unit's type locality as seen in our CTX mosaic are shown in Fig.
268 8. For a general photogeologic overview of the Hellas basin floor including this study's working
269 area, as well as more in-depth descriptions and interpretations of units *Hih*, *Hik*, and *HNila*
270 please see *Bernhardt et al. (2016a)*.

271 ## 5.1. Amazonian veneers

272 ***TARs*** **–** Fields of up to few 10s of meters wide "transverse aeolian ridges" (*Bourke et al.,*
273 *2003*). Often occur within local depressions. Orientations are variable, with dune fields on the
274 floor of the HPT occurring perpendicular as well as parallel with respect to the HPT's
275 topographic outlines. Within some occurrences, dunes tend to bend towards topographic
276 obstacles.

277 ***Scalloped*** **–** Fields of rimless, often elongate, and shallow depressions with diameters

between few 10s of meters and ~6.6 km. Occur mostly within craters > ~2 km diameter, but also within other local depressions. Orientations vary, but steepest slopes tend to occur on the northwestern inner walls. Often associated with *smooth* terrain.

Skeleton terrain – Relatively small patches of terrain characterized by 10s of meters to few 100s of meter large enclosures formed by irregularly shaped ridges. Mostly occurring within craters < 10 km diameter; often associated with *scalloped* terrain or *concentric crater fill*.

Concentric crater fill – Terrain exclusively occurring within craters and characterized by crater-concentric, often lobate lineations often manifested by small, meter-scale ridges. Average spacing of lineations is 50-100 m. Often associated with *scalloped* and *brain terrains*.

Brain terrain – Rough terrain characterized by up to 10s of meters wide knobs often forming a brain or coral-like texture. Mostly occurring within local topographic lows, e.g., between the hills of the hummocky interior formation. Often associated with *smooth* terrain.

Smooth – Surface appearing mostly featureless at scale of CTX mosaic (12 m/px). Often, but not exclusively, within local topographic lows. Often associated with *scalloped* and *brain terrains*.

Interpretation: The Amazonian veneers group within our mapping area consists of thin (< few 10s of meters) units formed by atmospheric outfall/redistributions driven by persistent winds moving through the Hellas basin in a clockwise pattern (*Siili et al., 1999; Ogohara and Satomura, 2008; Howard et al., 2012*). While large eolian constructs are absent, volatile-poorer materials accumulate as small *TARs* or settle down to form up to few 10s of meters thick *smooth* layers also referred to as "latitude-dependent mantle" (e.g., *Schon et al., 2012*). Volatile-richer materials, which might have been mobilized during past obliquity excursions (e.g., *Laskar et al., 2004*), tend to be preserved in wind traps, e.g., craters, and later become characterized by desiccation (*scalloped, skeleton terrain, brain terrain) (*e.g., *Zanetti et al., 2010; Levy et al., 2010*) and slope creep features (*concentric crater fill*) (*Levy et al., 2009, 2010).*

5.2. Crater materials

Fluidized ejecta – Concentric, mostly comprehensive deposit around craters extending up to ~2 crater diameters beyond the rim. Often with finger-like extensions, lobate onlaps, and radial lineations formed by decameter-scale striations, i.e., furrows and ridges (Fig. 6). Five craters (diameters ~1.5 to ~6 km; randomly scattered over mapping area) are surrounded by double- or multiple-layered fluidized ejecta. Smallest crater with mapped fluidized ejecta is ~1 km in diameter and located on interior formation close to northern map limit. One ~1.5 km crater with fluidized ejecta occurs on floor of Peneus Palus.

Non-fluidized ejecta – All circum-crater deposits that generally lack distinctive characteristics of fluidized ejecta as described above.

Crater material (undivided) – Morphologically distinct and sufficiently extensive (at mapping scale) crater rims as well as remnant central mounds/peaks, e.g., in Beloha crater.

Interpretation: Crater ejecta with a fluidized appearance are attributed to melting of subsurface ice by the energy released during the impact (e.g., *Mouginis-Mark, 1981*). Double- or multiple-layer ejecta specifically indicate target layers of different volatile-contents, either as permafrost (e.g., *Barlow and Perez,* 2003), and/or as surface ice (*Weiss and Head, 2013*). The occurrence of small craters (~1 km diameter) with fluidized ejecta suggests a target that was relatively ice-rich up to a depth of ~100 m or less at the time of impact (e.g., *Melosh, 1989*).

5.3. Thick mantling

Mantle – Corresponds to "mantle material (dark)" as mapped by *Bernhardt et al. (2016a)*. Outline often appears as a padded drop-off of up to ~100 m. Nearly featureless at scale of CTX-mosaic (12m/px); dissected by several kilometer-scale, shallow, elongate depressions that are aligned mostly parallel to the HPT outline. Often associated with *polygonal ridges*.

Polygonal ridges – Corresponds to "reticulate terrain 2" and "polygonal member" as mapped by *Diot et al. (2015)* and *Bernhardt et al. (2016a)*, respectively. Consists of up to ~8 km wide, but mostly less than ~2 km wide polygons formed by up to ~100 m high and few 10s

of meters wide linear to slightly curvilinear ridges.

Interpretation: The thick mantling is an order of magnitude thicker than the *smooth* material (latitude-dependent mantling; e.g., *Schon et al., 2012; Willmes et al., 2012*) and also appears to be distinctly older due to several km-sized, superposing craters. Mostly along its northeastern limit, the thick mantle transitions into the polygonal ridges, thereby indicating them to be clastic dikes previously contained in, and now being eroded out of, the once volatile-rich mantle (*Bernhardt et al., 2016a*). This, as well as deflation pit-like depressions suggest the thick mantling to currently undergo eolian erosion and possibly be mostly or entirely desiccated. As was proposed for similarly or even much thicker mantle deposits elsewhere, the thick mantling in the HPT might have been emplaced by snowfall during obliquity excursions within the Amazonian (e.g., *Head et al., 2006; Pedersen and Head, 2010*). This is in agreement with the absolute model age of 2.2 to 3.3 Ga we derived for the main occurrence of the *mantle* material (see supplementary online material 1).

5.4. Banded terrain

Banded terrain (BT) (ridged/cusp/convoluted/creviced) – The characteristics of the banded terrain have been described in detail in previous studies (e.g., *Diot et al., 2015; Bernhardt et al., 2016b, Voelker et al., 2017*) and can be summarized as follows: The banded terrain is a unique landform covering over 30,000 km² of the northwestern Hellas basin floor that consists of a smooth surface (at meter-scale) dissected by up to ~30 m deep, crevice-like, curvilinear troughs ("inter-bands") at a median spacing of few 100s of m. These troughs form various patterns, e.g., lobate/lamella-like or circular arrangements, but also confined zones of convolution with decameter-scale folding.

In our map (Fig. 2A), the banded terrain covers 30,071 km² and is divided into two subtypes: The creviced type (light blue/grey; 20,277 km²), which expresses the characteristics described above; and the ridged type (navy blue; 8,405 km²), which has a somewhat rougher

surface (at meter-scale) but shows the same general texture, albeit produced by ridges with the same dimensions as the curvilinear troughs of the creviced type (Fig. 5A). In some locations, ridged type areas appear to superpose creviced type areas (Fig. 5B, white arrows). The remainder of the banded terrain includes separately mapped zones of convolution (1,351 km²), which mostly occur as triangle- or wedge-shaped areas among the creviced type. Lastly, 382 km² constitute 11 small areas, which we refer to as "cusps" - apparently upthrust slabs and/or textures of intense, local-scale displacement sufficient to leave a topographic signature (as determined by shadows; Fig. 5D,E).

Boudinage-like band segmentations can be observed within creviced type areas (Fig. 5B, black arrows) and individual bands of the banded terrain appear to interact in both, brittle and ductile manners (e.g., Fig. 5C). Comparisons of MOC-NA with HiRISE images taken up to 14 years apart (e.g., E2001405 and ESP_045349_1405) show no discernible change within the banded terrain (e.g., collapse by de-volatilization or slope processes). The banded terrain superposes the honeycomb terrain (e.g., partially filling several honeycomb cells) as well as the hummocky, more elevated interior formation of the Hellas basin. Along its transition to the lower HPT in the northwestern basin, the material of the interior formation appears as elongate mesas (dark blue in Fig. 2A) embayed by banded terrain. In many locations, band orientations are aligned to the mesas, or terminate on one side and continue on the other (Fig. 5F). Several large crater ejecta (yellow in Fig 2A; e.g., around craters Beloha and Kufstein) superpose the banded terrain. In certain locations, e.g., north of Kufstein crater at 57.66°E, 35.67°S, ejecta appears to be dissected by bands of the underlying banded terrain (Fig. 6).

According to our grid mapping (Fig. 3) the orientation of bands does not seem to correlate with the local slope. All grid box categories (Fig. 3 and 4) are nearly equally abundant and distributed randomly, except within the honeycomb cells (circular arrangements dominant) and in the northernmost extents (lobate/slope-perpendicular arrangements dominant). In general, the banded terrain occurs across an elevation spectrum of over 2 km, from -7667 m up to -5548

m (Fig. 7B). Within this spectrum (Fig. 7B inlet), the creviced type follows a quasi-Gaussian distribution (mode at ~ -6765 m), whereas the ridged type occurs mostly below ~ -7,000 m (mode at ~ -7285 m).

Interpretation: See sections 6.3 and 6.4.

5.5. Interior formation

Hih **–** Corresponds to "hummocky member of the interior formation" (Hih) as mapped by *Bernhardt et al. (2016a)*. Characterized by 5-10 km wavelength roughness created by rounded hills and undulating mesas with padded rims. Widespread coverage by Amazonian veneers.

Hik **–** Corresponds to "knobby member of the interior formation" (Hik) as mapped by *Bernhardt et al. (2016a)*. Fields of 100s of meters to few kilometers wide knobs; often associated with *Hih*.

Fan-shaped **–** Four occurrences of roughly semicircular areas characterized by few 10s of meters-scale roughness created by radial lineations. Largest measures ~20 x 20 km, other three are less than ~5 x 10 km and ~4 x 4 km. On two largest occurrences, decameter-scale ridges forming braided patterns are visible. *Fan-shaped* landforms have little relief, but are always situated on top of *mesas* at distal (topographically lower) terminus of a sinuous ridge (Fig. 9).

Mesa/deformed mesa **–** Roughly based on "etched material" (He) as mapped by *Bernhardt et al. (2016a)*. Elevated, flat-topped areas with relatively sharp edges dropping ~100 to ~200 m down to surroundings. Mostly around highly degraded ~90 km wide crater in southern mapping area. Here, a system of braided, decameter-scale ridges can be seen on a ~19 x 11 km large *mesa* at 54.03°E; 40.12°S. *Mesas* often occur as few 100s of meters to few kilometers wide ridges, mostly radial to said crater (Fig. 9). Can appear "deformed", i.e., streamlined or striated in curvilinear patterns conforming to surrounding banded terrain. Contrary to stratigraphic interpretation of etched material by *Bernhardt et al. (2016a), mesas/deformed mesas* do not superpose *Hih*, but are superposed by it (Fig. 10A).

405 ***HNila*** **–** Corresponds to "arcuate, layered member of the interior formation" (HNila) as
406 mapped by *Bernhardt et al. (2016a)*. Flat-topped, step-like, up to ~150 m thick outcrops of
407 light-toned, horizontal, decameter-scale layers. CRISM data, e.g., FRT0000978A,
408 compromised by atmospheric effects. Within mapping area, occurs in two highly degraded
409 craters at similar elevation of ~ -7,000 m; largest occurrence close to Hellas basin center
410 (*Bernhardt et al., 2016a*). Superposed by all adjacent units.

411 **Interpretation:** Following the interpretation offered by *Bernhardt et al. (2016a)*, we
412 suggest the interior formation of the Hellas basin, mainly units *Hih* and *Hik*, but possibly also
413 the *mesas/deformed mesas*, to represent different erosional stages of Hesperian (~3.7 Ga
414 absolute model age) deposits derived from Hesperia Planum and the "Hesperia-Hellas trough",
415 where they might have been mobilized by hydrovolcanic processes. *HNila* might either be a
416 more pristine member of these deposits, or is a remnant of materials laid down earlier by
417 different, more localized processes, e.g., as sediments in a glacio-lacustrine environment that
418 was confined to the Hellas basin center as well as the two craters in western Hellas in which
419 *HNila* is found in (*Bernhardt et al., 2016a; Voelker et al., 2017*). Such a scenario would also
420 be in agreement with an interpretation of the sinuous ridges consisting of *mesa* material around
421 a partially *HNila*-filled, degraded crater (Fig. 9) as glaciofluvial or fluvial features, i.e., eskers
422 or inverted stream deposits. The *fan-shaped* deposits located at the distal termini of four of these
423 sinuous ridges are strongly reminiscent of terrestrial sandurs/outwash plains (braided ridge
424 system on largest two occurrences as well as directly on *mesa* superposed by smaller two
425 occurrences; e.g., *Benn and Evans, 2010*) and alluvial fans (radial striations on smaller two
426 occurrences, possibly remnants of tributary systems; e.g., *Ritter and Ten Brink, 1986*). This
427 indicates that glaciofluvial deposition might have taken place both, in subglacial as well as
428 proglacial settings, possibly as a sequence due to glacial retreat, with hydraulic drainage
429 transporting meltwater from a body of ice occupying (parts of) the floor of the degraded crater
430 amongst others. Furthermore, we suggest that such glacial activity might have been responsible

for the formation of the banded terrain (see section 6.4).

5.6. Plains materials

Etched (western) **–** Variable unit characterized by rough to knobby materials (100s of meters to kilometer-scale roughness) exclusively occurring on the southern floor of the HPT. Superposes *etched* and *fractured* units, superposed by all other adjacent units.

Etched **–** Similar to *etched (western),* albeit with larger topographic variations (up to ~400 m). Exclusively occurs on northern floor of HPT; superposes *rough* and *HC rim* units; superposed by all other adjacent units.

Rough (undivided) **–** Variable unit including low-relief, hummocky surfaces with several 100s of meters-scale roughness, as well as plains with ~50-200 meters-scale roughness. At least five occurrences of up to ~35 km long, ~400 m wide, degraded, flat-topped, sinuous ridges forming braided pattern in one location (56.98°E; 34.34°S). Ridges reside on *rough (undivided)* unit of northern HPT floor, but appear to emerge out of *etched* materials. Unit *rough (undivided)* exposed in various locations across the entire HPT floor; superposes *fractured* (Fig. 10B) and *HC rim* units, superposed by all other adjacent units.

Fractured **–** Smooth plains characterized by up to ~300 m wide, shallow, graben-like, solitary fractures often forming zig-zag patterns. Exclusively occurs on southern floor of HPT; superposed by all adjacent units (Fig. 10B).

Interpretation: The plains materials of this study's map largely correspond to the units HNpr (southern HPT) and $Npwr_{1/r}$ (northern HPT) of the photogeologic map by *Bernhardt et al. (2016a).* Accordingly, we interpret them as Noachian (~3.8 Ga absolute model age) basalt plains that are covered by relatively friable materials, which are likely to be remnants of *Hih/mesa material* and/or Hellas rim deposits (*Bernhardt et al., 2016a*). Missed by previous investigations but revealed by comprehensive CTX data, some of these remnants form sinuous ridges on the northern floor of the HPT, which might have been laid down as stream deposits

(fluvial) or eskers (subglacial). In any case, they postdate potential fluvial sediments and landforms along the inner wall of the nearby northern Hellas basin rim (units Nli and Nld by *Bernhardt et al. (2016a)*), as these rim deposits are superposed by the floor of the HPT. Instead, the sinuous ridges might be associated with the later formation of the interior formation (*Hih, Hik, mesas, HNila*), thereby indicating that its deposition involved (glacio-) fluvial activity.

5.7. Honeycomb terrain

Honeycomb rims (HC rims) **–** Approximately 1-2 km wide, up to ~170 m high ridges arranged in honeycomb-like pattern, i.e., forming edge-on-edge assemblage of circular to kidney/cell-shaped enclosures with a median diameter of ~7 km. Subdivided into three categories based on different morphologies. 1) *Furrowed*: Ridges are covered with ~80-400 m wide, up to few km long secondary ridges at a spacing of several 100s of meters. Areas between secondary ridges are *lineated*. Predominantly occur in central portion of honeycomb terrain. 2) *Bulged*: Ridges have rounded crests and steeper walls than other two categories. Occasionally dissected by up to 1 km wide, shallow, ridge-parallel troughs. Exclusively occur in northeastern honeycomb terrain. 3) *Lineated*: Ridges are flat-topped with slightly raised edges; meter to decameter-scale lineations (small ridges and troughs) occur on their tops, mostly parallel to ridge outlines, but can have turbulent texture at junction of three ridges (e.g., at 53.97°E; 37.97°S). Exclusively occur in southwestern honeycomb terrain.

Interpretation: In general, we adapt the interpretation of the so called honeycomb terrain as the surface expression of a diapir canopy, specifically withdrawal basins created by ridges of upwelling material (e.g., *Bernhardt et al., 2016b; Weiss et al., 2017*), which was elaborated on in further detail in section 3. The honeycomb terrain is manifested as mostly flat-floored enclosures bound by ridges. Both, the floors as well as the ridges show different morphologies, with the former being covered by different types of units also occurring outside the honeycomb terrain, e.g., *rough*, *etched*, *Hik*, and banded terrain (Fig. 10C). This was interpreted as filling

of the cells, thereby implying the honeycomb terrain to predate the plains material, for which an absolute model age of ~3.8 Ga was derived (*Bernhardt et al., 2016a,b*). The apparent geographic sequence of different HC rim categories (*lineated-furrowed-bulged* from SW to NE) might be caused by differential erosion across the honeycomb terrain, likely by persistent winds moving clockwise through the Hellas basin (*Howard et al., 2012*). Alternatively, the rim categories might be the surface expressions of different regimes of honeycomb formation, i.e., changing displacement kinematics between the honeycomb cells, possibly due to different rheologies within the overburden material (e.g., basalt vs. sandstone). This interpretation would be in agreement with turbulent textures on *lineated* HC rims, which occur at triple-junctions of honeycomb cells, which is also where turbulent displacement textures are seen in overburden materials of terrestrial salt or batholith diapir provinces (*Ramsay, 1989; Bouhallier et al., 1995; Jackson et al., 1990*). While the distinct basin-range landscape of the honeycomb terrain occurs only on Peneus Palus (i.e., the northern floor of the HPT), its general surface pattern (quasi-circular, ~5-10 km wide cells) extends beyond the ~1 km high scarp leading onto the interior formation. Here, the pattern is not expressed morphologically, but merely by the arrangement of convoluted zones within the banded terrain (Fig. 11). As already suggested by *Bernhardt et al. (2016b)* and further explained in section 6.4, we interpret this as a superposition effect caused by zones of convolution having preferentially formed above topographic rises, e.g., buried honeycomb rims, during the formation of the banded terrain.

6. Discussion

6.1. GPR and hyperspectral investigations

MARSIS/SHARAD: Neither MARSIS nor SHARAD revealed any definite reflectors beneath the Hellas basin (see supplementary online material 2). Several MARSIS tracks, e.g., R_10934_SS3, traverse the Hellas basin including the HPT and show horizontal reflectors further to the south, beneath the well-known south polar layered deposits (SPLD; e.g., *Plaut et*

506 *al., 2007*), but also beneath adjacent Promethei Planum. Beneath the honeycomb terrain,
507 SHARAD radargram QDA_7470010000 shows at least four slanted, several km long echoes at
508 depths between 1 and 2 km that are not seen in the respective simulation. However, as the
509 simulations are based on relatively low-resolution topography data by MOLA, these signals are
510 more likely to be surface clutter missed by the simulated radargram than actual reflectors. If the
511 signals are true reflectors, they would be in agreement with a salt or ice diapir-interpretation of
512 the honeycombs as they could represent reflections of well-developed, slanted diapir flanks.
513 Their depths of 1-2 km would accommodate either material scenario, salt as well as ice, for
514 which overburden thicknesses in that range have been predicted (*Bernhardt et al., 2016b, Weiss*
515 *and Head, 2017*).

516 While GPRs have been successfully used to detect halite and water ice interfaces in the
517 subsurfaces of Earth and Mars (e.g., *Stewart and Unterberger, 1976; Annan et al., 1988; Plaut*
518 *et al., 2007; Orosei et al., 2015*), the lack of detectable, definite reflectors beneath the
519 honeycomb terrain can have various reasons: 1) Hellas' rough surface creates intense radar
520 clutter, thus greatly reducing GPR sensitivity (*Seu et al., 2007; Orosei et al., 2015*). 2) An
521 upwelling layer can develop diapirs with near-vertical flanks (e.g., *Diegel et al., 1995*), i.e.,
522 non-horizontal reflectors that are very difficult to detect from orbit. 3) Certain interfaces, e.g.,
523 between dry halite and sandstone, have small dielectric contrasts resulting in very weak
524 reflections (*National Research Council, 2000*).

525 **CRISM:** Despite atmospheric corrections (see Data and techniques), all 12 analyzed
526 CRISM scenes (nine FRTs including one new pre-projected/processed MTRDR image + three
527 HRL/HRS; all covering the banded terrain, *HC rims*, or unit *HNila*) are characterized by a
528 ubiquitous CO_2 signature. A very weak, ubiquitous H_2O ice signature can be seen in certain
529 images (e.g., HRS00010EF1) alongside strong CO_2 absorption features. Certain spectral
530 parameters, e.g., "D2300" defined by a 2.3 µm drop-off, which can be indicative of
531 hydroxylated silicates (*Viviano-Beck et al., 2014*) but also of CO_2 (*Hansen, 1997*), do show a

spatial correlation with outcrops within the banded terrain (e.g., on FRT0000AAD1; see supplementary online material 3). However, averaged spectra of these "signatures" only show the afore mentioned CO_2 features and become virtually flat when ratioed with a nearby, spectrally bland reference area, which, in turn, indicates an atmospheric signal. Thus, we explain the spatial correlation with the fact that outcrops, i.e., steep slopes, are usually associated with shadows, where an increased fraction of the CRISM signal comes from the atmosphere instead of the surface, thereby intensifying the atmospheric signature (including the relatively weak 2.3 µm drop-off for CO_2).

6.2. Stratigraphic model

Based on our 1:175,000 morphologic map (Fig. 2A) and MOLA data, we derived stratigraphic profiles along three traverses (Fig. 12). The map unit groups *honeycomb terrain* and *plains materials* as well as the units *mesa/deformed mesa* (Fig. 2B) are represented by a single stratigraphic unit, respectively.

Our self-consistent stratigraphic model is based on interpretations of the honeycomb terrain as the surface expression of a diapir canopy as well as the banded terrain as a partially superposing thin veneer. It is consistent with the models by *Bernhardt et al. (2016a,b)* based on those studies' 1:2,000,000 map with one exception: Our comprehensive CTX observations showed the *mesa/deformed mesa* units to be superposed by the hummocky interior unit *Hih* (Fig. 10A). Based on THEMIS observations, *Bernhardt et al. (2016a)* interpreted this relationship to be inverted, i.e., *Hih* to underlie the "etched material", which corresponds to the *mesa* units. It is thus possible that a large volume of the westernmost Hellas interior formation is in fact composed of *mesa* material and not *Hih*. Based on the unconsolidated and rounded appearance of *Hih*, it might represent a reworked form (deflation/mass wasting) of the *mesa* material, which is exposed only along the erosive environment of the HPT (*Howard et al., 2012; Bernhardt et al., 2016a*).

Timing of the banded terrain: The banded terrain is superposed on the *honeycomb terrain*, the *plains materials* and on *the interior formation*, for which model ages between 3.8 and 3.7 Ga were derived (*Bernhardt et al., 2016a*). It is superposed by the *thick mantling, crater materials* and *Amazonian veneers*. While the latter two did not lend themselves to reliable crater size-frequency measurements, we derived an absolute model age of 2.2 to 3.3 Ga for the main occurrence of the *mantle* material (see supplementary online material). This implies that banded terrain formation took place between ~3.7 and ~2.2 Ga, which is in agreement with *Diot et al.'s (2014)* derived crater retention age of ~3 Ga. However, it is noteworthy that banded terrain activity/deformation appears to have persisted or recurred, at least locally, after crater accumulation had begun, as it dissected otherwise well-preserved, superposing crater ejecta, e.g., north of Kufstein crater (Fig. 6).

6.3. What is the banded terrain?

As already mentioned in section 3, interpretations of the banded terrain have been diverse, yet always implied some form of viscous deformation to explain its curvilinear, folded patterns. Earlier studies equated or associated the banded and honeycomb terrains, suggesting the former to be deeply rooted material that was viscously displaced by compressive stresses during honeycomb formation (e.g., *Moore and Wilhelms, 2001; Mangold and Allemand., 2003, Kite et al., 2009*). However, *Diot et al. (2014, 2015a,b)* and *Bernhardt et al., (2016b)* observed potential (peri)-glacial features on the banded terrain's surface such as pingo-/sublimation pit-like landforms, disintegration into brain terrain, and "slabs" detaching from its main body (see section 3). These features, as well as the banded terrain occurring up to 100s of kilometers away from the honeycombs, cast an immediate genetic association (i.e., a joint formation by the same process) into doubt. Instead, they seemed to imply a thin veneer scenario of gravity-driven, ductile deformation of volatile-rich material postdating the honeycombs. The new findings of our investigation are in agreement with an interpretation of the banded terrain as a relatively

582 thin layer that underwent ductile deformation at or near the surface: 1) Cusps indicating thin
583 layer buckling (Fig. 5D,E); 2) the banded terrain's spread over an elevation spectrum of ~2 km
584 (Fig. 7); as well as 3) its occurrence on the flanks of intact, non-deformed ridges of likely
585 (glacio-)fluvial origin (Fig. 9). However, based on our observations, we offer further
586 refinements of the banded terrain's nature and origin, arguing against deformation by gravity-
587 driven, downslope flow.

588 The ubiquitous, curvilinear, decameter to kilometer-scale folding of the banded terrain
589 implies a relatively uniform, viscous behavior in the past. Furthermore, while our investigation
590 of CRISM data did not reveal any clear surface signatures, three observations tentatively
591 indicate the current banded terrain to consist of relatively volatile-poor, heterogeneous material:
592 1) Outcrops and fresh crater ejecta containing up to decameter-scale blocks (*Diot et al., 2015b*)
593 but lacking any fluidization features; 2) a generally elevated, yet variable THEMIS-based
594 thermal inertia; and 3) a lack of detectable surface change (e.g., collapse or mass wasting) on
595 MOC-NA-HiRISE image pairs taken up to 14 years (~7.4 Mars years) apart. Shallow, i.e., not
596 deeply-rooted, terrestrial materials known to form and preserve (via cooling or
597 desiccation/cementation) ductile, decameter- as well as kilometer-scale, curvilinear
598 deformation patterns at or near the surface include low viscous materials like salt, lava, and
599 ice/ice-rich material (e.g., *Talbot, 1979; Lockwood et al., 1987; Bevington and Copland, 2014*).

600 **Salt:** As was previously elaborated, deeply-rooted halokinetic sequences exposed around
601 many salt diapirs on Earth (e.g., *Jackson et al., 1990*) contradict the observation-based thin
602 veneer-interpretation of the banded terrain. Nevertheless, so called "salt glaciers" (Fig. 12A),
603 i.e., several 10s to few 100s of meters thick, downslope creeping sheets of salt originating from
604 diapirs are common in terrestrial salt provinces (*Talbot, 1979; Jackson et al., 1990; Fletcher et*
605 *al., 1995*) and can even contain water dissolution features reminiscent of certain thermokarst
606 landforms observed on the banded terrain (*Talbot, 1979; Jackson et al., 1990*). Furthermore,
607 assuming them to be the result of salt diapirs, the adjacent honeycombs would be suitable

608 sources of salt. However, while subaerial salt glaciers can produce up to decameter-scale
609 curvilinear patterns (e.g., *Talbot, 1979*), neither them nor submarine salt glaciers (*Fletcher et*
610 *al., 1995*) are known to create kilometer-scale patterns even remotely similar to the banded
611 terrain. Moreover, fold patterns within salt glaciers develop according to downslope creep
612 (*Talbot, 1979*), which is not in agreement with our grid map showing no correlation between
613 slope and band orientation (Fig. 3).

614 **Lava:** Curvilinear patterns are occasionally formed on solidifying lava sheets, e.g., the up
615 to kilometer-scale pattern formed by meter-scale flow fronts during the 1984 fissure eruption
616 in the central caldera of Mauna Loa, Hawai'i (Fig. 13B; *Lockwood et al., 1987*). Although these
617 textures can be reminiscent of the ridged type banded terrain (e.g., Fig 4D), we argue against
618 such an interpretation as no volcanic landforms, e.g., potential vents/fissures, flows, or calderas,
619 have been identified anywhere on the Hellas basin floor (e.g., *Williams et al., 2010, Bernhardt*
620 *et al., 2016a*). Moreover, unlike flow fronts on lava sheets/flows, the orientations of bands in
621 most locations of the banded terrain does neither conform to the outlines of apparently embayed
622 materials nor correlate to the local topography. Lastly, the dominant creviced type
623 (characterized by curvilinear troughs; Fig. 3, 4C, 5C,D), as well as potential (peri-)glacial
624 features of the banded terrain (e.g., thermokarst-like depressions and disintegration into brain
625 terrain), lack any correspondence on the surfaces of terrestrial or martian lava sheets.

626 **Ice/ice-rich material:** On Earth, curvilinear, decameter- to kilometer-scale surface
627 patterns including isoclinal folds can be found on ice shelves (e.g., *Crabtree and Doake, 1980*)
628 and on surge glaciers (e.g., *Bevington and Copland, 2014)*. In both cases, they occur in
629 recurrently fast-moving ice at junctions of interacting stress fields, e.g., along the edge of the
630 Ross ice shelf, Antarctica (Fig. 13C), or at the confluence of a tributary glacier and the main
631 ice tongue of Dusty Glacier in Kluane National Park, Yukon/Canada (Fig. 13D). Unlike Dusty
632 Glacier, whose curvilinear texture is spatially confined and directly determined by gravity-
633 driven flow, ice shelf patterns are only indirectly created by gravity-driven flow of their source

glaciers on land (*Casassa et al., 1991*). They can extend over several 10s of kilometers as they are an immediate result of ductile deformation along shear- and compaction zones at the shelf margin (*Crabtree and Doake, 1980; Rignot et al., 2011*). The result can be surface patterns and morphologies that are very reminiscent of the banded terrain, e.g., kilometer-scale, tapering, crevice-like troughs, isoclinal folds, cusp-forming buckling (Fig. 13C, black arrow), and confined zones of intense, smaller-scale deformation. Moreover, ice shelf margins produce ductile as well as brittle deformation in close geographic association, e.g., slab break-off and rotation (Fig. 13C, white arrow), or one slab breaking through another slab, which itself is being flexed. Such arrangements are also common in the banded terrain, where intact slabs apparently broke through other slabs (Fig. 5C, white arrow) or folding was partially accommodated by brittle failure and flexural slip (Fig. 5C, black arrow). In ice shelves, these phenomena are enabled by multiple stress fields that result in spatially varied strain rates acting on a decoupled lid, which might, thus, imply a similar setup during the deformation of what today is the banded terrain. However, if the banded terrain had also been decoupled due to floatation on a past body of water, we would not expect its fine-scale texture to be preserved while it settled down on a rugged landscape across an elevation spectrum of over 2 km during the recession of an ice- and debris-covered sea. Furthermore, while the banded terrain is a prominent landscape with a relatively fresh appearance, no other landforms indicative of a past, standing body of water on the Hellas basin floor have been identified (*Bernhardt et al., 2016a; Voelker et al., 2017*), thus further casting an ice shelf model into doubt.

6.4. A glacial formation model

Despite the inadequacy of an ice shelf model, we submit that a formation of the banded terrain's texture due to ice/ice-rich material being deformed by multiple local-scale stress fields remains a promising concept. The general pattern of bands in the banded terrain implies numerous, small-scale, slope-independent stress fields (<10s of km) of different orientations.

As no regional pattern (>10s of km) can be identified within the banded terrain, we suggest that large/regional-scale stress fields, either by tectonics or long-wavelength topography, had little or no effect on its deformation. One terrestrial analog setting with local stress fields deforming a wet/ice-rich layer is a wet-based, subglacial environment, in which low viscous, ice/water-rich till is deformed in stress fields caused by the ice overburden pressure (Fig. 14; e.g., *Boulton et al., 1974; Alley et al., 1986*). Various different strain rates can result from the overburden pressure acting in conjunction with bed topography, as well as from zones of variable surging and basal decoupling created by ice flow patterns primarily governed by regional bed topography but also by the hydraulic transmissibility of the bed as determined by its geology (*Brennand, 2000; Margold et al., 2015*). Such variable strain rates might account for the different curvatures and spacings of bands in the banded terrain, and could potentially explain its zones of convolution. Due to their often "curly" appearance, we interpret these zones to be indicative of intense compression and shearing, which, in a subglacial scenario, would be expected in association with topographic obstacles as well as a low hydraulic transmissibility of the glacier bed (e.g., *Boulton et al., 1974; Margold et al., 2015*). Thus, as the zones of convolution are often arranged in patterns mimicking the adjacent honeycombs (Fig. 11), it is possible that they are located above buried honeycomb-cell rims, which affected the stress field applied to the glacial substrate. Such a causal relationship between bed topography and banded terrain deformation would explain several locations, where band orientations conform to embayed, elongate *mesas* (Fig. 5F) and/or appear to have deformed/streamlined (partially) superposed *mesas*. The two sections of the banded terrain, where band orientations correlate more with modern topography (its northernmost extents as well as within most honeycombs; Fig. 3), might, in turn, indicate a locally stronger contribution of gravity-driven flow, possibly due to their location close to the northern ice sheet margin, i.e., beneath a much thinner ice overburden. A glacial formation model for the banded terrain might also be in agreement with the sinuous ridges we identified in the southern part of our morphologic map and that are always

685 located on broader rises being unconformably superposed by banded terrain (Fig. 9). As larger-
686 scale topographic rises of the glacier bed are often associated with a reduced ice thickness, i.e.,
687 smaller overburden pressure resulting in a negative hydraulic gradient, they are a preferred
688 location of terrestrial esker-forming drainage tunnels (*Shreve, 1985; Ashley et al., 1991*). Thus,
689 we prefer an interpretation of the sinuous ridges as deposits by subglacial drainage. Moreover,
690 the braided ridges on elevated areas often occurring at the distal termini of the sinuous ridges
691 (Fig. 9B, lower left) constitutes a landform sequence also found on Earth, and might have
692 formed as sandurs/outwash plains immediately beyond the glacier margin (*Shreve, 1985;*
693 *Brennand, 2000; Benn and Evans, 2010*).

694 In order to preserve the intricate banded patterns in its substrate, the glacier had to retreat
695 in a mostly stagnant fashion, potentially due to sublimation. This might have been driven by
696 katabatic winds, which models suggest to descend from Malea Planum and be pervasive
697 throughout the HPT (*Siili, 1999; Howard et al., 2012*), therefore also explaining the banded
698 terrain's apparent desiccation. Hence, we interpret the ridged type of the banded terrain as wind-
699 degraded version of the creviced type, with the ridges being clastic dikes of material that once
700 filled the crevices (Fig. 5A). This is in agreement with the ridged type predominantly occurring
701 in the lowest elevations of the unit's extent (Fig. 7), where deflation is expected to be more
702 intense, possibly including saltation and abrasion (*Siili, 1999; Howard et al., 2012*). Lastly, it
703 was noted that intense deflation over few 10s of millions of years by such winds could be
704 responsible for the exposure of the deep lying, ancient honeycombs, thus offering an
705 explanation for the geographic association between the unique banded and honeycomb terrains
706 (*Bernhardt et al., 2016a,b*).

707 However, a remaining problem of such a subglacial formation model is the lack of
708 kilometer-scale, curvilinear textures in respective terrestrial analog environments (*Boulton et*
709 *al., 1974*). Therefore, we cannot conclusively demonstrate its suitability to explain the origin of
710 the banded terrain.

Climatic considerations: Due to its low elevation and relatively low latitude on the southern hemisphere, the Mars Climate Database (MCD; *Forget et al. 1999; Millour et al. 2015*) predicts that no other location on Mars experiences temperatures and pressures as high and for as long (per Mars year) as the HPT. Daily maximum temperatures of at least 273 K are maintained throughout a third of the year, while pressures are above 10 mbar for more than half the day during this time. However, without decisive atmospheric changes, even obliquity excursions to 45° only predict increased dust lifting in Hellas and ice precipitation for the eastern Hellas basin rim, but no decisive changes in mean ground temperature and pressure that would enable ice accumulation in the HPT (*Haberle et al., 2003*; *Forget et al., 2006; Wordsworth, 2016*). Nevertheless, as it is likely that atmospheric pressures were still higher during the early Amazonian (*Madeleine et al., 2009; Read et al., 2015*), ice sheets on the Hellas basin floor might have been sustainable, e.g., as distal reaches of glaciers originating in accumulation zones within the adjacent basin rim. This specific topographic setup might also explain why the banded terrain is unique on Mars, while HPT-like climatic conditions are and have been occurring elsewhere, yet in much more confined areas, e.g., in Lyot crater, lacking comparable potential ice accumulation zones.

7. Main results and conclusions

Based on our 1:175,000 map (159,856 km²) of northwest Hellas Planitia, we assessed the morphologic inventory and stratigraphy of the area at a resolution that resolves the constituents of the banded and honeycomb terrains. Amazonian deposits are widespread, with recent veneers, e.g., smooth and brain terrain, covering ~23% and superposing different types of crater materials (e.g., ejecta) 8% of the map area. Late Hesperian to Amazonian thick mantling, covering 14% including associated degradation products, are superposed by several craters and show a CSFD-derived absolute model age range of 2.2 to 3.3 Ga. The banded terrain covers 19% and is partially superposed by thick mantling, crater ejecta, as well as Amazonian veneers,

736 while it superposes the interior formation (16%), plains materials (17%), and honeycomb
737 terrain. Based on our analyses, as well as previous investigations (*Bernhardt et al., 2016a,b;*
738 *Voelker et al., 2017)*, we laid out a comprehensive, self-consistent stratigraphic model, which
739 incorporates the banded terrain as relatively thin surface layer and the honeycomb terrain as the
740 surface expression of evolved diapirs.

741 **Honeycomb terrain:** In agreement with previous studies, we conclude the honeycombs to
742 be ancient structures, as they are partially filled and/or covered by different materials of the
743 adjacent plains and interior formation (absolute model ages ~3.8 Ga and ~3.7 Ga; *Bernhardt et*
744 *al. 2016a*). Within the honeycomb terrain, we differentiated three rim categories (lineated-
745 furrowed-bulged from SW to NE). Following their interpretation as surface expressions of salt
746 or ice diapirs (*Bernhardt et al., 2016b; Weiss and Head, 2017*), these categories might reflect a
747 transition of formation regimes, e.g., displacement kinematics during diapir ascent due to
748 variable overburden geology. As radar (MARSIS/SHARAD) and hyperspectral data (CRISM)
749 did not reveal any definite reflectors and surface signatures beneath and on it, respectively, we
750 were not able to characterize the honeycomb terrain in further detail.

751 **Banded terrain:** The banded terrain covers 30,071 km² across an elevation spectrum of
752 over 2 km, from -7667 m up to -5548 m. It can be subdivided into two types, creviced and
753 ridged. Since it dominates the lowest areas, where deflation is expected to be more intense (e.g.,
754 *Howard et al., 2012*), we interpret the ridged type as degraded version of the creviced type. The
755 banded terrain partially fills several honeycombs, but also occurs up to ~240 km away from the
756 honeycomb terrain, e.g., on ridges of likely (glacio-)fluvial origin. Based on these observations
757 and those by previous investigations (see section 3), we conclude the banded terrain cannot be
758 a deeply rooted unit but has to be a relatively thin surface layer. As it superposes the interior
759 formation of the Hellas basin (~3.7 Ga, *Bernhardt et al., 2016a*), but is partially covered by
760 thick mantling, for which we derived an absolute model age range between 2.2 and 3.3 Ga, a
761 Hesperian/early Amazonian age is implied for the banded terrain. Our grid mapping of the

762 banded terrain showed no regional band pattern or correlation between band orientations and
763 local topography, and we conclude that neither regional-scale tectonics nor gravity-driven
764 downslope flow played a major role during its formation. While CRISM data revealed no
765 distinct surface signatures for the entire region, HiRISE, MOC-NA, and THEMIS observations
766 indicate the modern banded terrain to consist of relatively volatile-poor, heterogeneous material
767 containing decameter-scale blocks. Based on regional geomorphology and terrestrial analogs,
768 we argue against salt or volcanic deposits as its main constituents. Instead we tentatively
769 propose a subglacial formation, involving viscous deformation of wet/ice-rich till by small-
770 scale stress fields created by an interplay of ice overburden pressure on local topography.
771 Models and observations indicate persistent katabatic winds in the area, which might later have
772 removed the glacier and desiccated the exposed substrate. While terrestrial analogs of such
773 settings are not known to produce kilometer-scale, curvilinear textures, a scenario like this
774 would be in agreement with sinuous, esker-like ridges and sandur-like, elevated plains, whose
775 flanks are partially superposed by the banded terrain, and, thus, might indicate an involvement
776 of glacial activity during its emplacement. Although the validity of the proposed formation
777 model cannot be conclusively demonstrated, we submit that potential future CRISM
778 observations detecting unambiguous signatures, e.g., of chlorides (salts?) or phyllosilicates
779 (sediments?), on the cusps and convoluted zones of the banded terrain, would be the most
780 promising, currently feasible contribution to understand this enigmatic landscape.

8. Table

Group	Unit	Type locality (°E; °S)	Area (km²)
Amazonian veneers (23%)	*1) TARs*	59.31; 34.08	705
	2) Scalloped	55.00; 41.42	2804
	3) Skeleton terrain	58.07; 35.98	75
	4) Concentric crater fill	53.45; 37.00	187
	5) Brain terrain	59.21; 36.36	5916
	6) Smooth	53.28; 43.52	26623
Crater materials (8%)	*7) Fluidized ejecta*	57.36; 38.77	8433
	8) Non-fluidized ejecta	58.01; 33.78	2886
	9) Crater material	51.29; 40.65	1055
Thick mantling (14%)	*10) Mantle*	52.21; 38.58	18368
	11) Polygonal ridges	58.02; 36.61	4312
Banded terrain (19%)	*12) BT (ridged)*	52.04; 41.73	8405
	13) BT (cusps)	53.51; 39.13	38
	14) BT (convoluted)	56.15; 37.84	1351
	15) BT (creviced)	52.26; 40.39	20277
Interior formation (16%)	*16) Hih**	60.69; 35.66	7220
	*17) Hik**	60.75; 36.01	3139
	18) Fan-shaped	54.10; 40.19	244
	19) Mesa (deformed)	57.28; 37.81	3795
	20) Mesa	58.24; 37.43	10766
	*21) HNila**	53.15; 41.15	541
Plains materials (17%)	*22) Etched (western)*	50.80; 41.17	4566
	23) Etched	57.98; 34.01	7072
	24) Rough (undivided)	51.78; 36.99	14421
	25) Fractured	52.48; 42.87	645
Honeycomb terrain (4%)	*26) HC rim (furrowed)*	56.65; 36.45	2954
	27) HC rim (bulged)	58.16; 34.99	2304
	28) HC rim (ridged)	53.90; 37.95	758

Table 1: Unit groups (and map area percentage), unit names, type localities, and areal extents of all units of our morphologic map (Fig. 2). Standardized images of each type locality are shown in Fig. 8. * unit labels adopted from *Bernhardt et al. (2016a)*.

9. References

Alley, R. B., Blankenship, D. D., Bentley, C. R., & Rooney, S. T. (1986). Deformation of till beneath ice stream B, West Antarctica. *Nature*, *322*(6074), 57–59. http://doi.org/10.1038/322057a0

Annan, A. P., Davis, J. L., & Gendzwill, D. (1988). Radar sounding in potash mines, Saskatchewan, Canada. *Geophysics*, *53*(12), 1556–1564. http://doi.org/10.1190/1.1442437

Ashley, J. W., Boothroyd, J. C., & Borns, H. W. (1991). Sedimentology of late Pleistocene (Laurentide) deglacial-phase deposits, eastern Maine: An example of a temperate marine grounded ice-sheet margin. In J. B. Anderson & G. M. Ashley (Eds.), *Glacial marine sedimentation; Paleoclimatic significance* (pp. 107–127). Boulder: The Geological Society of America.

Barlow, N. G., & Perez, C. B. (2003). Martian impact crater ejecta morphologies as indicators of the distribution of subsurface volatiles. *Journal of Geophysical Research*, *108*(E8), 5085. http://doi.org/10.1029/2002JE002036

Benn, D. I., & Evans, D. J. A. (2010). *Glaciers and Glaciation* (2nd ed.). New York City: Hodder Education. Retrieved from https://books.google.de/books/about/Glaciers_and_Glaciation.html?id=c0xNAQAAIAAJ&redir_esc=y

Bernhardt, H., Hiesinger, H., Ivanov, M. A., Ruesch, O., Erkeling, G., & Reiss, D. (2016a). Photogeologic mapping and the geologic history of the Hellas basin floor, Mars. *Icarus*, *264*, 407–442. http://doi.org/10.1016/j.icarus.2015.09.031

Bernhardt, H., Reiss, D., Hiesinger, H., & Ivanov, M. A. (2016b). The honeycomb terrain on the Hellas basin floor, Mars: A case for salt or ice diapirism. *Journal of Geophysical Research: Planets*, *121*(4), 714–738. http://doi.org/10.1002/2016JE005007

Bevington, A., & Copland, L. (2014). Characteristics of the last five surges of Lowell Glacier, Yukon, Canada, since 1948. *Journal of Glaciology*, *60*(219), 113–123. http://doi.org/10.3189/2014JoG13J134

Bouhallier, H., Chardon, D., & Choukroune, P. (1995). Strain patterns in Archaean dome-and-basin structures: The Dharwar craton (Karnataka, South India). *Earth and Planetary Science Letters*, *135*(1–4), 57–75. http://doi.org/10.1016/0012-821X(95)00144-2

Boulton, G. S., Dent, D. L., & Morris, E. M. (1974). Subglacial Shearing and Crushing, and the Role of Water Pressures in tills from South-East Iceland. *Geografiska Annaler. Series A, Physical Geography*, *56*(3/4), 135. http://doi.org/10.2307/520703

Bourke, M. C., Wilson, S. A., & Zimbelman, J. R. (2003). The Variability of Transverse Aeolian Ripples in Troughs on Mars. In *Lunar and Planetary Science Conference* (p. 2009). The Woodlands, Texas.

823 Brennand, T. A. (2000). Deglacial meltwater drainage and glaciodynamics: inferences from
824 Laurentide eskers, Canada. *Geomorphology*, *32*(3), 263–293. Retrieved from
825 http://neogeo.kent.edu/munro/glacial/Brennand_Tracy_A.pdf

826 Cantini, F., Pio Rossi, A., Orosei, R., Baumann, P., Misev, D., Oosthoek, J., Beccati, A.,
827 Campalani, P., Unnithan, V. (2014). MARSIS data and simulation exploited using array
828 databases: PlanetServer/EarthServer for sounding radars. *EGU General Assembly*
829 *Conference Abstracts* 16, 3784.

830 Casassa, G., Jezek, K. C., Turner, J., & Whillans, I. M. (1991). Relict flow stripes on the Ross
831 Ice Shelf. *Annals of Glaciology*, *15*, 132–138.

832 Crabtree, R. D., & Doake, C. S. M. (1980). Flow lines on Antarctic ice shelves. *Polar Record*,
833 *20*(124), 31. http://doi.org/10.1017/S0032247400002898

834 Diegel, F. A., Karlo, J. F., & Schuster, D. C. (1995). Cenozoic structural evolution and
835 tectono-stratigraphic framework of the northern Gulf Coast continental margin. *AAPG*
836 *Memoir*, *65*, 109–151. Retrieved from
837 http://archives.datapages.com/data/specpubs/memoir65/ch06/0109.htm

838 Diot, X., El-Maarry, M. R., Schlunegger, F., Norton, K. P., Thomas, N. H., & Grindrod, P. M.
839 (2014). The geomorphology and morphometry of the banded terrain in Hellas basin,
840 Mars. *Planetary and Space Science*, *101*, 118–134.
841 http://doi.org/10.1016/j.pss.2014.06.013

842 Diot, X., El-Maarry, M. R., Guallini, L., Schlunegger, F., Norton, K. P., Thomas, N. H., …
843 Grindrod, P. M. (2015a). An ice-rich flow origin for the banded terrain in the Hellas
844 basin, Mars. *Journal of Geophysical Research: Planets*, *120*(12), 2258–2276.
845 http://doi.org/10.1002/2015JE004956

846 Diot, X., El-Maarry, M. R., Schlunegger, F., Norton, K. P., Thomas, N. H., Grindrod, P. M.,
847 & Chojnacki, M. (2015b). Complex geomorphologic assemblage of terrains in
848 association with the banded terrain in Hellas basin, Mars. *Planetary and Space Science*,
849 *121*, 36–52. http://doi.org/10.1016/j.pss.2015.12.003

850 Edwards, C. S., Nowicki, K. J., Christensen, P. R., Hill, J., Gorelick, N., & Murray, K. (2011).
851 Mosaicking of global planetary image datasets: 1. Techniques and data processing for
852 Thermal Emission Imaging System (THEMIS) multi-spectral data. *Journal of*
853 *Geophysical Research*, *116*(E10), E10008. http://doi.org/10.1029/2010JE003755

854 Fletcher, R. C., Hudec, M. R., & Watson, I. A. (1995). Salt glacier and composite sediment-
855 salt glacier models for the emplacement and early burial of allochthonous salt sheets. In
856 M. P. A. Jackson, D. G. Roberts, & S. Snelson (Eds.), *Salt tectonics: a global*
857 *perspective* (Vol. 65, pp. 77–108).

858 Forget, F., Hourdin, F., Fournier, R., Hourdin, C., Talagrand, O., Collins, M., … Huot, J.-P.
859 (1999). Improved general circulation models of the Martian atmosphere from the surface
860 to above 80 km. *Journal of Geophysical Research: Planets*, *104*(E10), 24155–24175.
861 http://doi.org/10.1029/1999JE001025

Forget, F., Haberle, R. M., Montmessin, F., Levrard, B., & Head, J. W. (2006). Formation of Glaciers on Mars by Atmospheric Precipitation at High Obliquity. *Science*, *311*(5759), 368–371. http://doi.org/10.1126/science.1120335

Hansen, G. B. (1997). The infrared absorption spectrum of carbon dioxide ice from 1.8 to 333 μm. *Journal of Geophysical Research: Planets*, *102*(E9), 21569–21587. http://doi.org/10.1029/97JE01875

Hartmann, W. K. (2005). Martian cratering 8: Isochron refinement and the chronology of Mars. *Icarus*, *174*(2), 294–320. http://doi.org/10.1016/j.icarus.2004.11.023

Head, J. W., Marchant, D. R., Agnew, M. C., Fassett, C. I., & Kreslavsky, M. A. (2006). Extensive valley glacier deposits in the northern mid-latitudes of Mars: Evidence for Late Amazonian obliquity-driven climate change. *Earth and Planetary Science Letters*, *241*(3–4), 663–671. http://doi.org/10.1016/j.epsl.2005.11.016

Heyer, T., Erkeling, G., Hiesinger, H., Reiss, D., Luesebrink, D., Bernhardt, H., & Jaumann, R. (2017). The multi-temporal database of planetary image data (MUTED): A tool to support the identification of surface changes on Mars. In *Lunar and Planetary Science Conference* (p. 1019).

Howard, A. D., Spiga, A., & Moore, J. M. (2012). The Deepest Basin on Mars is formed by Aeolian Erosion: Western Hellas Planitia. In *Lunar and Planetary Science Conference* (p. 1105).

Jackson, M. P. A., Cornelius, R. R., Craig, C. H., Gansser, A., Stöcklin, J., & Talbot, C. J. (1990). *Salt Diapirs of the Great Kavir, Central Iran*. The Geological Society of America. Retrieved from http://rock.geosociety.org/Store/detail.aspx?id=MWR177

Jackson, M. P. A., Cornelius, R. R., Craig, C. H., Gansser, A., Stöcklin, J., & Talbot, C. J. (1990). *Salt Diapirs of the Great Kavir, Central Iran*. The Geological Society of America. Retrieved from http://rock.geosociety.org/Store/detail.aspx?id=MWR177

Kadish, S. J., & Head, J. W. (2011). Impacts into non-polar ice-rich paleodeposits on Mars: Excess ejecta craters, perched craters and pedestal craters as clues to Amazonian climate history. *Icarus*, *215*(1), 34–46. http://doi.org/10.1016/j.icarus.2011.07.014

Kite, E. S., Manga, M., & Perron, J. T. (2009). Evidence for Past Kilometer-Scale Overturn (s) in Deformed, Layered Terrain Near the Deepest Point on Mars. In *Lunar and Planetary Science Conference* (p. 1249). Retrieved from http://adsabs.harvard.edu/abs/2009LPI....40.1248K

Laskar, J., Correia, A. C. M., Gastineau, M., Joutel, F., Levrard, B., & Robutel, P. (2004). Long term evolution and chaotic diffusion of the insolation quantities of Mars. *Icarus*, *170*(2), 343–364. http://doi.org/10.1016/j.icarus.2004.04.005

Levy, J. S., Head, J. W., & Marchant, D. R. (2009). Concentric crater fill in Utopia Planitia: History and interaction between glacial “brain terrain” and periglacial mantle processes. *Icarus*, *202*(2), 462–476. http://doi.org/10.1016/j.icarus.2009.02.018

Levy, J. S., Head, J. W., & Marchant, D. R. (2010). Concentric crater fill in the northern mid-latitudes of Mars: Formation processes and relationships to similar landforms of glacial origin. *Icarus*, *209*(2), 390–404. http://doi.org/10.1016/j.icarus.2010.03.036

Lockwood, J. P., Dvorak, J. J., English, T. T., Koyanagi, R. Y., Okamura, A. T., Summers, M. L., & Tanigawa, W. R. (1987). Mauna Loa 1974-1984: A decade of intrusive and extrusive activity. In *Volcanism in Hawaii* (pp. 537–570). U.S. Geological Survey. Retrieved from https://pubs.usgs.gov/pp/1987/1350/

Madeleine, J. B., Forget, F., Head, J. W., Levrard, B., Montmessin, F., & Millour, E. (2009). Amazonian northern mid-latitude glaciation on Mars: A proposed climate scenario. *Icarus*, *203*(2), 390–405. http://doi.org/10.1016/j.icarus.2009.04.037

Malin, M. C., Bell, J. F., Cantor, B. A., Caplinger, M. A., Calvin, W. M., Clancy, R. T., … Wolff, M. J. (2007). Context Camera Investigation on board the Mars Reconnaissance Orbiter. *Journal of Geophysical Research: Planets*, *112*(E5), E05S04. http://doi.org/10.1029/2006JE002808

Malin, M. C., & Edgett, K. S. (2010). An overview of the 1985-2006 Mars Orbiter Camera science investigation. *The Mars Journal*, *5*, 1–60. http://doi.org/10.1555/mars.2010.0001

Mangold, N., & Allemand, P. (2003). Ductile Deformation in Hellas Floor: Salt Diapirs or Crustal Domes? *International Conference on Mars*, 3047. Retrieved from http://www.lpi.usra.edu/meetings/sixthmars2003/pdf/3047.pdf

Margold, M., Stokes, C. R., & Clark, C. D. (2015). Ice streams in the Laurentide Ice Sheet: Identification, characteristics and comparison to modern ice sheets. *Earth-Science Reviews*, *143*, 117–146. http://doi.org/10.1016/j.earscirev.2015.01.011

McEwen, A. S., Eliason, E. M., Bergstrom, J. W., Bridges, N. T., Hansen, C. J., Delamere, W. A., … Weitz, C. M. (2007). Mars Reconnaissance Orbiter's High Resolution Imaging Science Experiment (HiRISE). *Journal of Geophysical Research: Planets*, *112*(E5), E05S02. http://doi.org/10.1029/2005JE002605

McGuire, P. C., Bishop, J. L., Brown, A. J., Fraeman, A. A., Marzo, G. A., Frank Morgan, M., … Wolff, M. J. (2009). An improvement to the volcano-scan algorithm for atmospheric correction of CRISM and OMEGA spectral data. *Planetary and Space Science*, *57*(7), 809–815. http://doi.org/10.1016/j.pss.2009.03.007

Melosh, H. J. (1989). *Impact cratering: A geologic process*. New York: Oxford University Press (Oxford Monographs on Geology and Geophysics, No. 11). Retrieved from http://adsabs.harvard.edu/abs/1989QB603.C7M45....

Michael, G., & Neukum, G. (2010). Planetary surface dating from crater size–frequency distribution measurements: Partial resurfacing events and statistical age uncertainty. *Earth and Planetary Science Letters*, *294*(3–4), 223–229. http://doi.org/10.1016/j.epsl.2009.12.041

Millour, E., Forget, F., Spiga, A., Navarro, T., Madeleine, J.-B., Montabone, L., … Huot, J.-P. (2015). The Mars Climate Database (MCD version 5.2). *Eighth International Conference on Mars*, *10*, 1184.

940 Moore, J. M., & Wilhelms, D. E. (2001). Hellas as a Possible Site of Ancient Ice-Covered
941 Lakes on Mars. *Icarus*, *154*(2), 258–276. http://doi.org/10.1006/icar.2001.6736

942 Moratto, Z. M., Broxton, M. J., Beyer, R. A., Lundy, M., & Husmann, K. (2010). Ames
943 Stereo Pipeline , NASA ' s Open Source Automated Stereogrammetry. *Lunar and*
944 *Planteary Science Conference*, 1–2.

945 Mouginis-Mark, P. J. (1981). Ejecta emplacement and modes of formation of martian
946 fluidized ejecta craters. *Icarus*, *45*(1), 60–76. http://doi.org/10.1016/0019-
947 1035(81)90006-3

948 Murchie, S. L., Arvidson, R. E., Bedini, P., Beisser, K., Bibring, J. P., Bishop, J. L., … Wolff,
949 M. J. (2007). Compact Reconnaissance Imaging Spectrometer for Mars (CRISM) on
950 Mars Reconnaissance Orbiter (MRO). *Journal of Geophysical Research: Planets*,
951 *112*(E5), E05S03. http://doi.org/10.1029/2006JE002682

952 National Research Council (2000). *Seeing into the Earth: Noninvasive Characterization of the*
953 *Shallow Subsurface for Environmental and Engineering Applications*. Washington, DC:
954 The National Academies Press. https://doi.org/10.17226/5786.

955 Nouvel, J.-F., Herique, A., Kofman, W., Safaeinili, A. (2004). Radar signal simulation:
956 Surface modeling with the Facet Method. *Radio Science* 39, RS1013.

957 Ogohara, K., & Satomura, T. (2008). Northward movement of Martian dust localized in the
958 region of the Hellas Basin. *Geophysical Research Letters*, *35*(13), L13201.
959 http://doi.org/10.1029/2008GL034546

960 Orosei, R., Jordan, R. L., Morgan, D. D., Cartacci, M., Cicchetti, A., Duru, F., … Picardi, G.
961 (2015). Mars Advanced Radar for Subsurface and Ionospheric Sounding (MARSIS) after
962 nine years of operation: A summary. *Planetary and Space Science*, *112*, 98–114.
963 http://doi.org/10.1016/j.pss.2014.07.010

964 Pedersen, G. B. M., & Head, J. W. (2010). Evidence of widespread degraded Amazonian-
965 aged ice-rich deposits in the transition between Elysium Rise and Utopia Planitia, Mars:
966 Guidelines for the recognition of degraded ice-rich materials. *Planetary and Space*
967 *Science*, *58*(14–15), 1953–1970. http://doi.org/10.1016/j.pss.2010.09.019

968 Picardi, G., Biccari, D., Seu, R., Plaut, J. J., Johnson, W. T. K., Jordan, R. L., … Zampolini,
969 E. (2004). MARSIS: Mars Advanced Radar for Subsurface and Ionosphere Sounding.
970 *European Space Agency, (Special Publication)*, (1240), 51–69. Retrieved from
971 https://www.scopus.com/record/display.uri?eid=2-s2.0-
972 4243089410&origin=inward&txGid=F149CCF2E2A635B4AE404B2E7ECF3ACA.wsn
973 Aw8kcdt7IPYLO0V48gA%3A1

974 Putzig, N. (2014). CPB : The CO-SHARPS Processing Boutique SHARAD Processors. In
975 *SHARAD/MARSIS Data Users' Workshop* (p. 30). Retrieved from http://pds-
976 geosciences.wustl.edu/workshops/SHARAD_MARSIS_Mar14/Putzig_CO-SHARPS-
977 Processing-Boutique.pdf

978 Ramsay, J. G. (1989). Emplacement kinematics of a granite diapir: the Chindamora batholith,
979 Zimbabwe. *Journal of Structural Geology*, *11*(1–2), 191–209.
980 http://doi.org/10.1016/0191-8141(89)90043-6

981 Read, P. L., Lewis, S. R., & Mulholland, D. P. (2015). The physics of Martian weather and
982 climate: a review. *Reports on Progress in Physics*, *78*(12), 125901.
983 http://doi.org/10.1088/0034-4885/78/12/125901

984 Rignot, E., Mouginot, J., & Scheuchl, B. (2011). Ice Flow of the Antarctic Ice Sheet. *Science*,
985 *333*(6048), 1427–1430. http://doi.org/10.1126/science.1208336

986 Ritter, D. F., & Ten Brink, N. W. (1986). Alluvial Fan Development and the Glacial-
987 Glaciofluvial Cycle, Nenana Valley, Alaska. *The Journal of Geology*, *94*(4), 613–625.
988 http://doi.org/10.1086/629063

989 Schon, S. C., Head, J. W., & Fassett, C. I. (2012). Recent high-latitude resurfacing by a
990 climate-related latitude-dependent mantle: Constraining age of emplacement from counts
991 of small craters. *Planetary and Space Science*, *69*(1), 49–61.
992 http://doi.org/10.1016/j.pss.2012.03.015

993 Shreve, R. L. (1985). Esker characteristics in terms of glacier physics, Katahdin esker system,
994 Maine. *Geological Society of America Bulletin*, *96*(5), 639. http://doi.org/10.1130/0016-
995 7606(1985)96<639:ECITOG>2.0.CO;2

996 Siili, T., Haberle, R. M., Murphy, J. R., & Savijarvi, H. (1999). Modelling of the combined
997 late-winter ice cap edge and slope winds in Mars Hellas and Argyre regions. *Planetary*
998 *and Space Science*, *47*(8–9), 951–970. http://doi.org/10.1016/S0032-0633(99)00016-1

999 Smith, M. D., Zuber, M. T., Frey, H. V., Garvin, J. B., Head, J. W., Muhleman, D. O., … Sun,
1000 X. (2001). Mars Orbiter Laser Altimeter: Experiment summary after the first year of
1001 global mapping of Mars. *Journal of Geophysical Research: Planets*, *106*(E10), 23689.
1002 http://doi.org/10.1029/2000JE001364

1003 Stewart, R. D., & Unterberger, R. R. (1976). Seeing through rock-salt with Radar.
1004 *Geophysics*, *41*(1), 123–132. http://doi.org/10.1190/1.1440595

1005 Talbot, C. J. (1979). Fold trains in a glacier of salt in southern Iran. *Journal of Structural*
1006 *Geology*, *1*(1), 5–18.

1007 Thomas, N. H., Beyer, R. A., Byrne, S., Moore, J. M., Wilson, S. A., Wray, J. J., & McEwen,
1008 A. S. (2010). The Banded Terrain in the NW Region of Hellas Basin. In *European*
1009 *Planetary Science Congress*.

1010 Viviano-Beck, C. E., Seelos, F. P., Murchie, S. L., Kahn, E. G., Seelos, K. D., Taylor, H. W.,
1011 … Morgan, M. F. (2014). Revised CRISM spectral parameters and summary products
1012 based on the currently detected mineral diversity on Mars. *Journal of Geophysical*
1013 *Research: Planets*, *119*(6), 1403–1431. http://doi.org/10.1002/2014JE004627

1014 Voelker, M., Hauber, E., Schulzeck, F., & Jaumann, R. (2017). Grid-mapping Hellas Planitia,
1015 Mars – Insights into distribution, evolution and geomorphology of (Peri)-glacial, fluvial

and lacustrine landforms in Mars' deepest basin. *Planetary and Space Science*, *145*, 49–70. http://doi.org/10.1016/j.pss.2017.07.012

Weiss, D. K., & Head, J. W. (2013). Formation of double-layered ejecta craters on Mars: A glacial substrate model. *Geophysical Research Letters*, *40*(15), 3819–3824. http://doi.org/10.1002/grl.50778

Weiss, D. K., & Head, J. W. (2017). Salt or ice diapirism origin for the honeycomb terrain in Hellas basin, Mars?: Implications for the early martian climate. *Icarus*, *284*, 249–263. http://doi.org/10.1016/j.icarus.2016.11.016

Willmes, M., Reiss, D., Hiesinger, H., & Zanetti, M. (2012). Surface age of the ice-dust mantle deposit in Malea Planum, Mars. *Planetary and Space Science*, *60*(1), 199–206. http://doi.org/10.1016/j.pss.2011.08.006

Wilson, S. A., Moore, J. M., Howard, A. D., & Wilhelms, D. E. (2010). Evidence for ancient lakes in the Hellas region. *In Lakes on Mars* (pp. 195–222). Elsevier. http://doi.org/10.1016/B978-0-444-52854-4.00007-6

Wordsworth, R. (2016). The Climate of Early Mars. *Annual Review of Earth and Planetary Sciences*, *44*(1), 381–408. http://doi.org/10.1146/annurev-earth-060115-012355

Zanetti, M., Hiesinger, H., Reiss, D., Hauber, E., & Neukum, G. (2010). Distribution and evolution of scalloped terrain in the southern hemisphere, Mars. *Icarus*, *206*(2), 691–706. http://doi.org/10.1016/j.icarus.2009.09.010

10. Figures

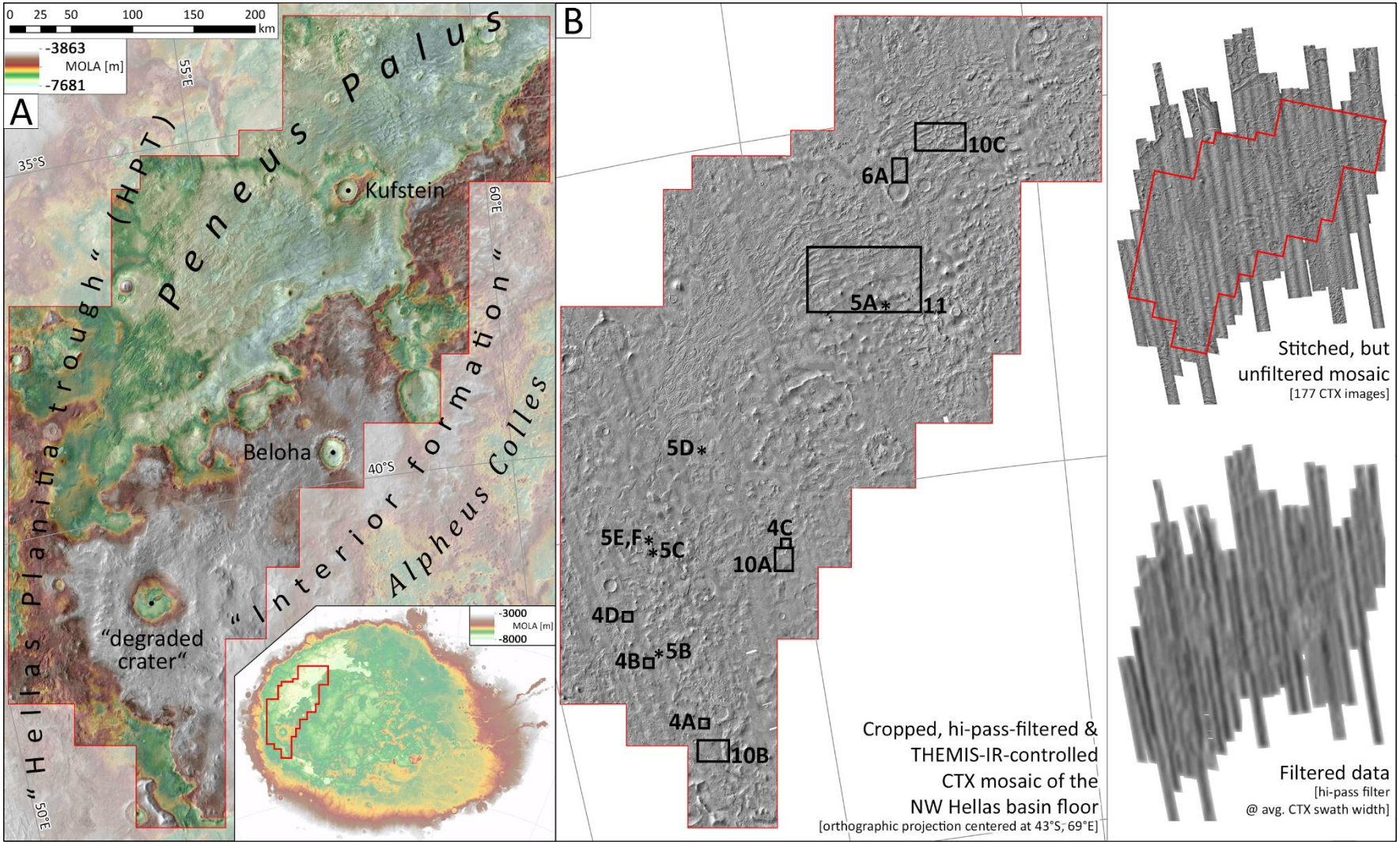
A
B
0 25 50 100 150 200 km
-3863
MOLA [m]
-7681
Peneus Palus
"Hellas Planitia trough" (HPT)
"Interior formation"
Alpheus Colles
Kufstein
Beloha
"degraded crater"
35°S
40°S
50°E
55°E
60°E
-3000
MOLA [m]
-8000
10C
6A
5A*
11
5D*
5E,F*
*5C
4C
10A
4D
4B
*5B
4A
10B
Cropped, hi-pass-filtered & THEMIS-IR-controlled CTX mosaic of the NW Hellas basin floor
[orthographic projection centered at 43°S, 69°E]
Stitched, but unfiltered mosaic
[177 CTX images]
Filtered data
[hi-pass filter @ avg. CTX swath width]

Figure 1: A) Physiographic overview of our mapping area on northwestern Hellas Planitia. MOLA DTM superposed on THEMIS-IR daytime mosaic (version 12). Inlet shows MOLA DTM of the entire Hellas basin floor; red outline indicates mapping area. B) Same scene showing our purpose-built CTX mosaic, which served as basemap for our morphologic map (Fig. 2), as well as two intermediate processing steps. Numbered asterisks and black boxes indicate locations of following figures.

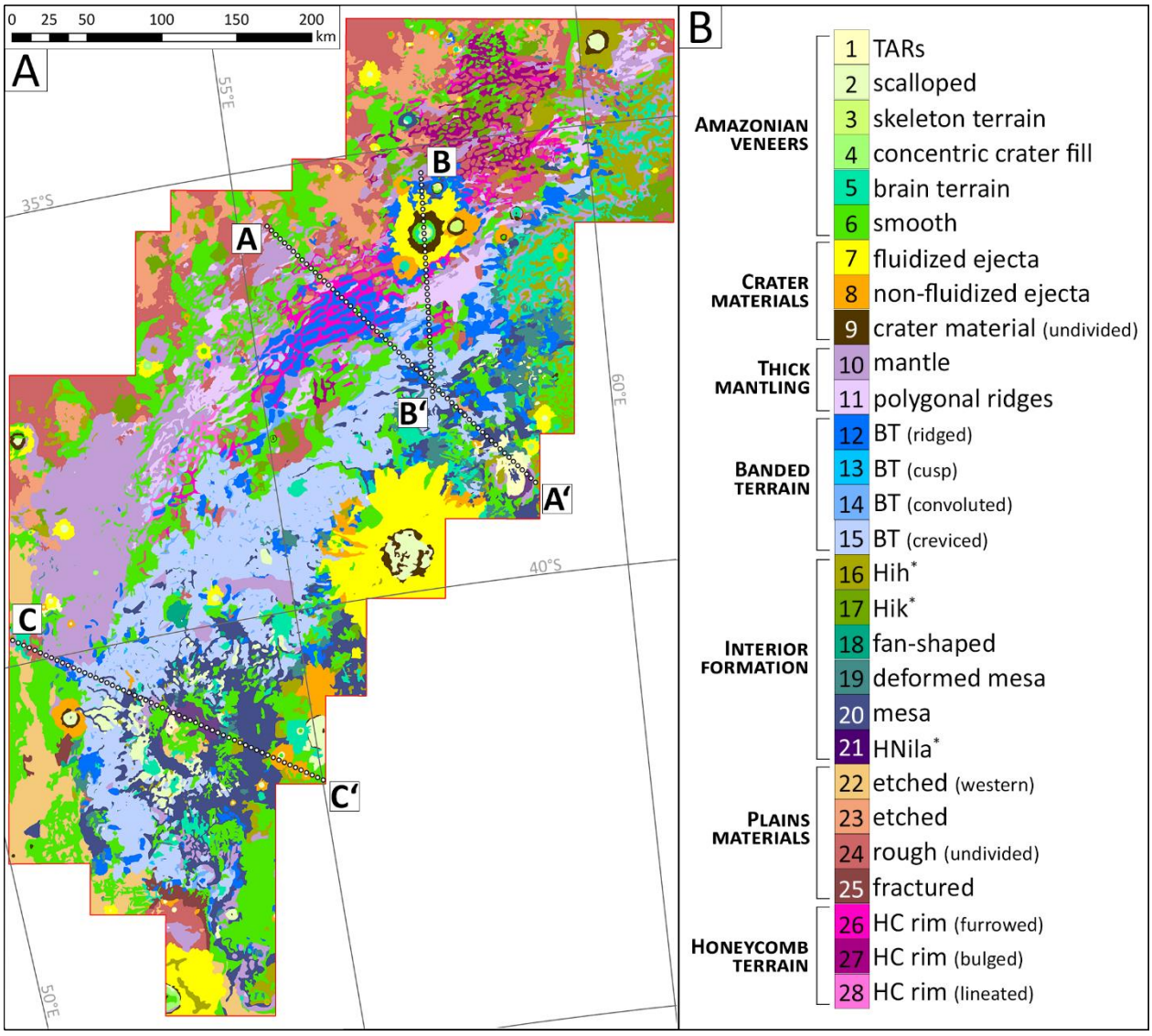

Figure 2: A) CTX-based, morphologic map (1:175,000) of northwestern Hellas Planitia (see Fig. 1A for context). Dotted white lines indicate traverses of stratigraphic profiles shown in Fig. 12. For descriptions and interpretations of all map units see section 5; unit type localities and areal extents are listed in table 1; standardized images of all type localities are shown in Fig. 8. B) Stratigraphically ordered and grouped list of all mapped units. * unit labels adopted from *Bernhardt et al. (2016a)*.

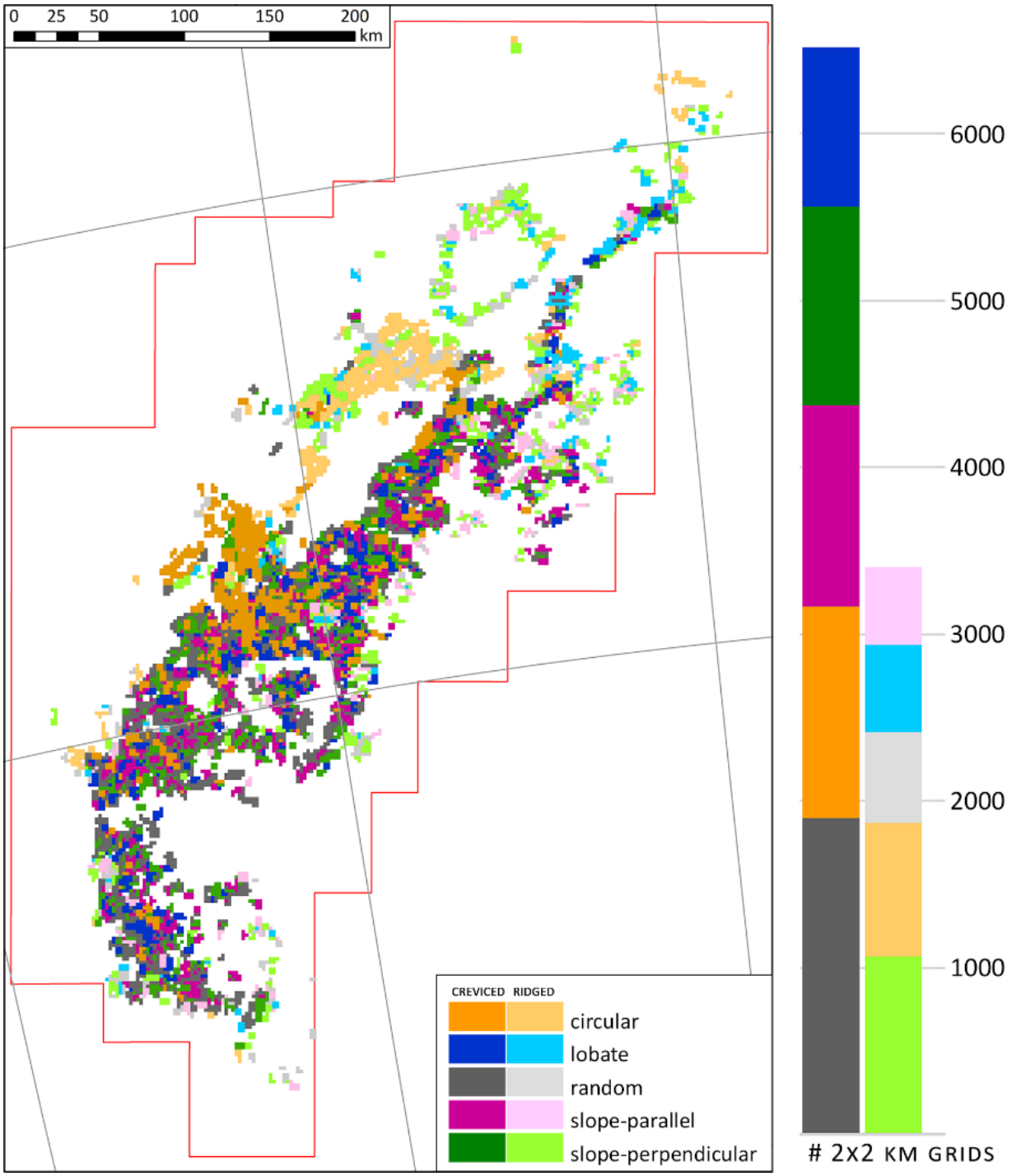

Figure 3: Grid mapping (box size 2x2 km) of the banded terrain as outlined in our morphologic map (Fig. 2). Colors indicate the dominant pattern of bands within a box (see inlet); color brightness shows the two different types of banded terrain (creviced and ridged). Bar chart compares absolute number of boxes per type and category. See Fig. 3 for illustrations of different grid categories.

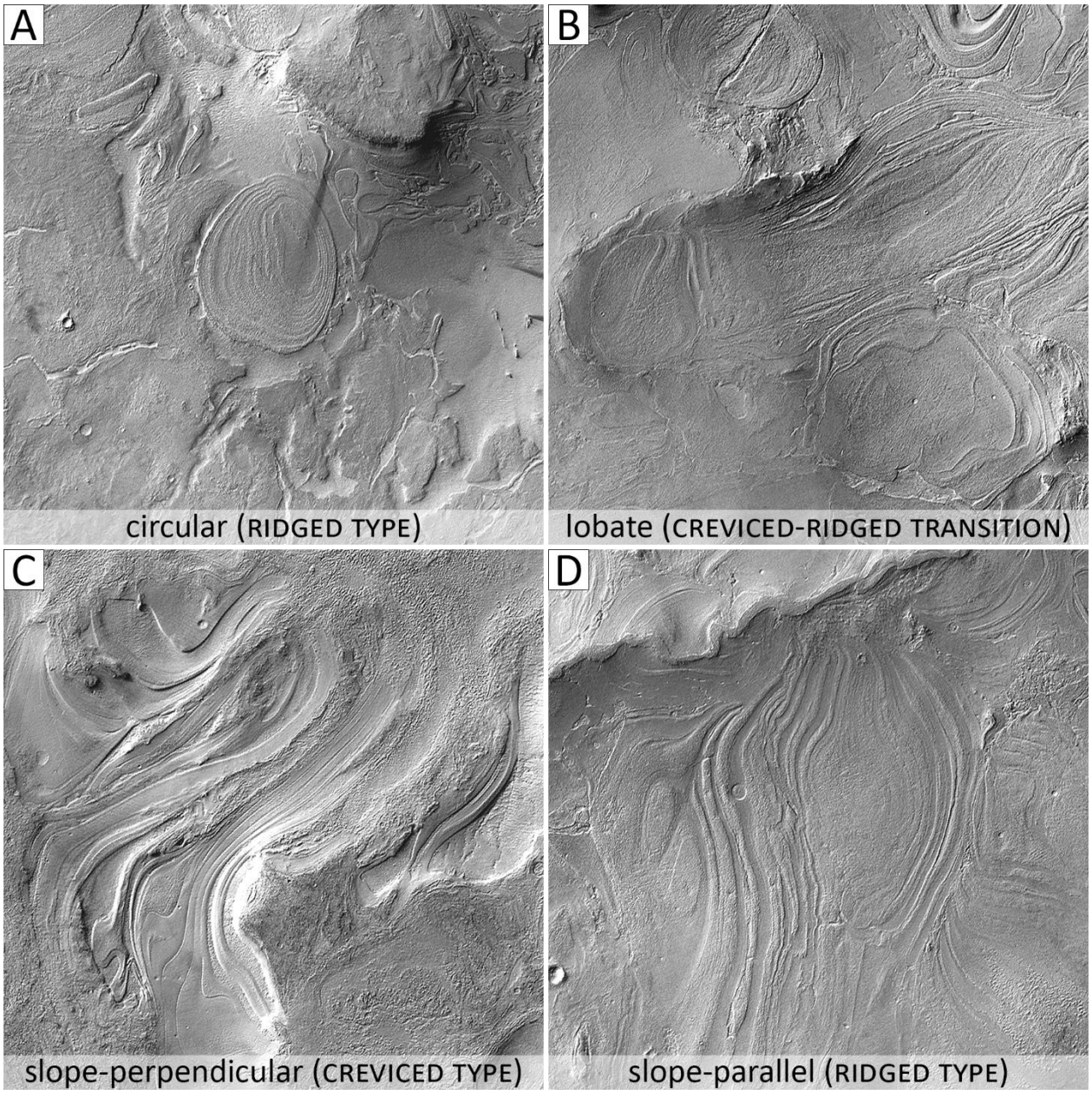

Figure 4: A-D) Collage of crops from our purpose-built CTX mosaic illustrating the four defined types of banded terrain patterns mapped in Fig. 3. Side lengths of images is 10 km; north is up; all image locations indicated in Fig. 1B.

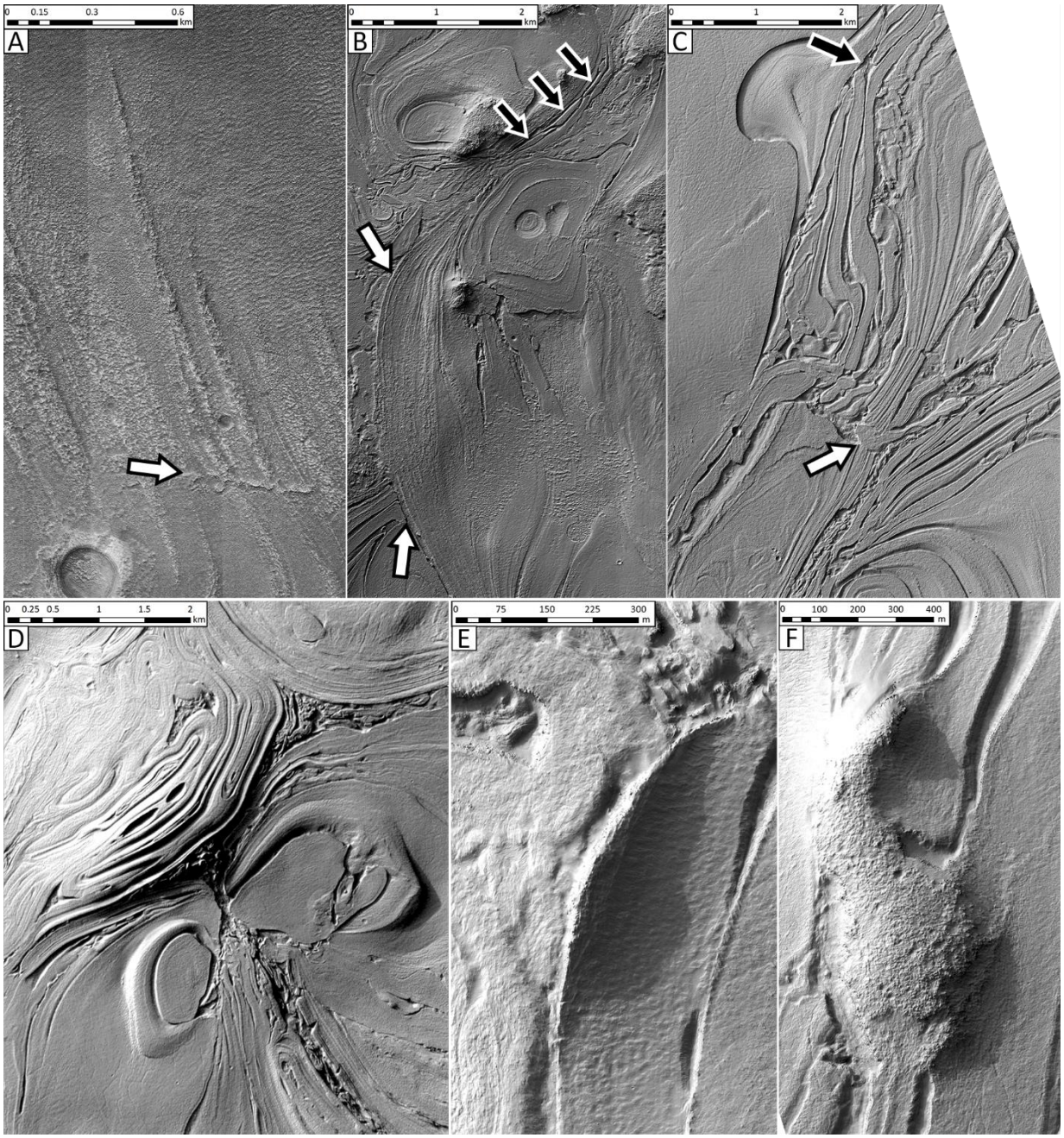

Figure 5: Detail observations of the banded terrain; all image locations indicated in Fig. 1B. A) HiRISE image ESP_019978_1420 showing a transition from creviced type banded terrain (south of white arrow) to the ridged type (north of white arrow). B) HiRISE image ESP_035116_1380 showing a braid-like portion of ridged type banded terrain apparently overlapping creviced type banded terrain (white arrows). Black arrows mark three boudinage-like segments within creviced typed banded terrain. C) HiRISE image PSP_008269_1395 of creviced type banded terrain; the

white arrow indicates one slab apparently breaking through another and causing the adjacent slab to rotate slightly; the black arrow marks band segmentation at a fold hinge, possibly enabling flexural slip. D) CTX image P13_006199_1382 showing a butterfly-shaped cusp. E) HiRISE image PSP_008269_1395 of a small ridge, probably a buckled slab, at the edge of a band of the creviced type banded terrain. F) HiRISE image PSP_008269_1395 of an inselberg-like, elongate mesa, which the surrounding band orientations appear to conform to.

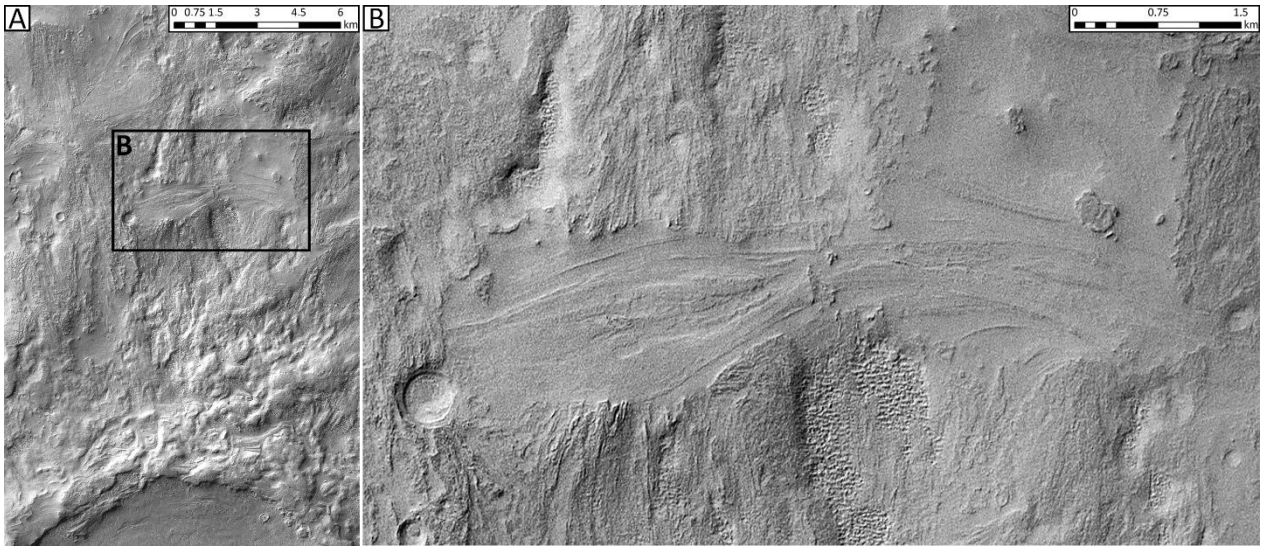

Figure 6: A) Crop of our CTX mosaic showing the northern rim of Kufstein crater (bottom of image) in the northern portion of our mapping area (location indicated in Fig. 1A). North is up. B) CTX image P16_007425_1443 showing a zoom on a portion of Kufstein's ejecta, which appears to be dissected by underlying banded terrain.

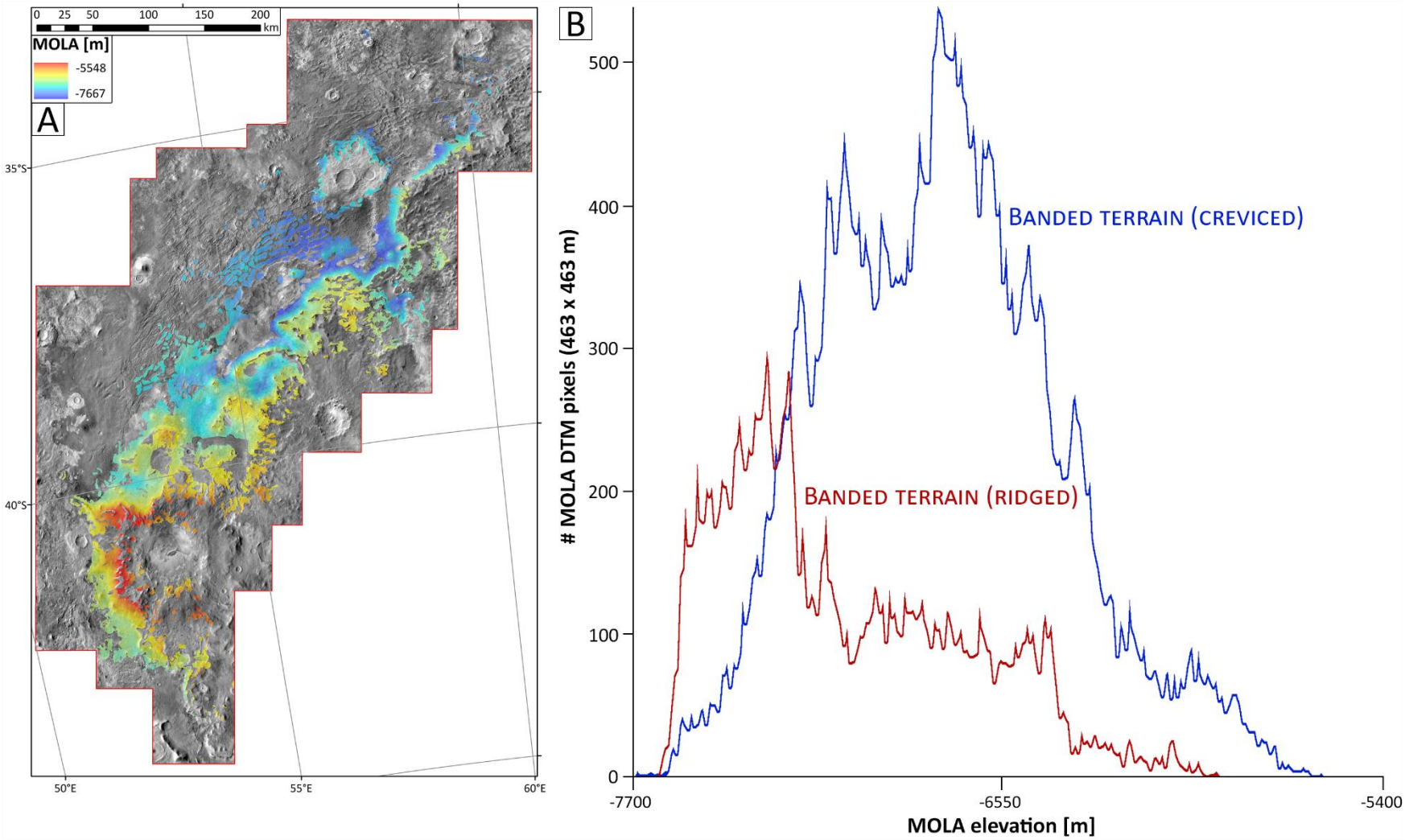

Figure 7: A) THEMIS-IR daytime mosaic overlain by MOLA DTM cut out according to the banded terrain outline as shown in our morphologic map (Fig. 2). B) Hypsogram of all MOLA DTM pixels (463 x 463 m) contained within the banded terrain and differentiated

according to its type (creviced and ridged).

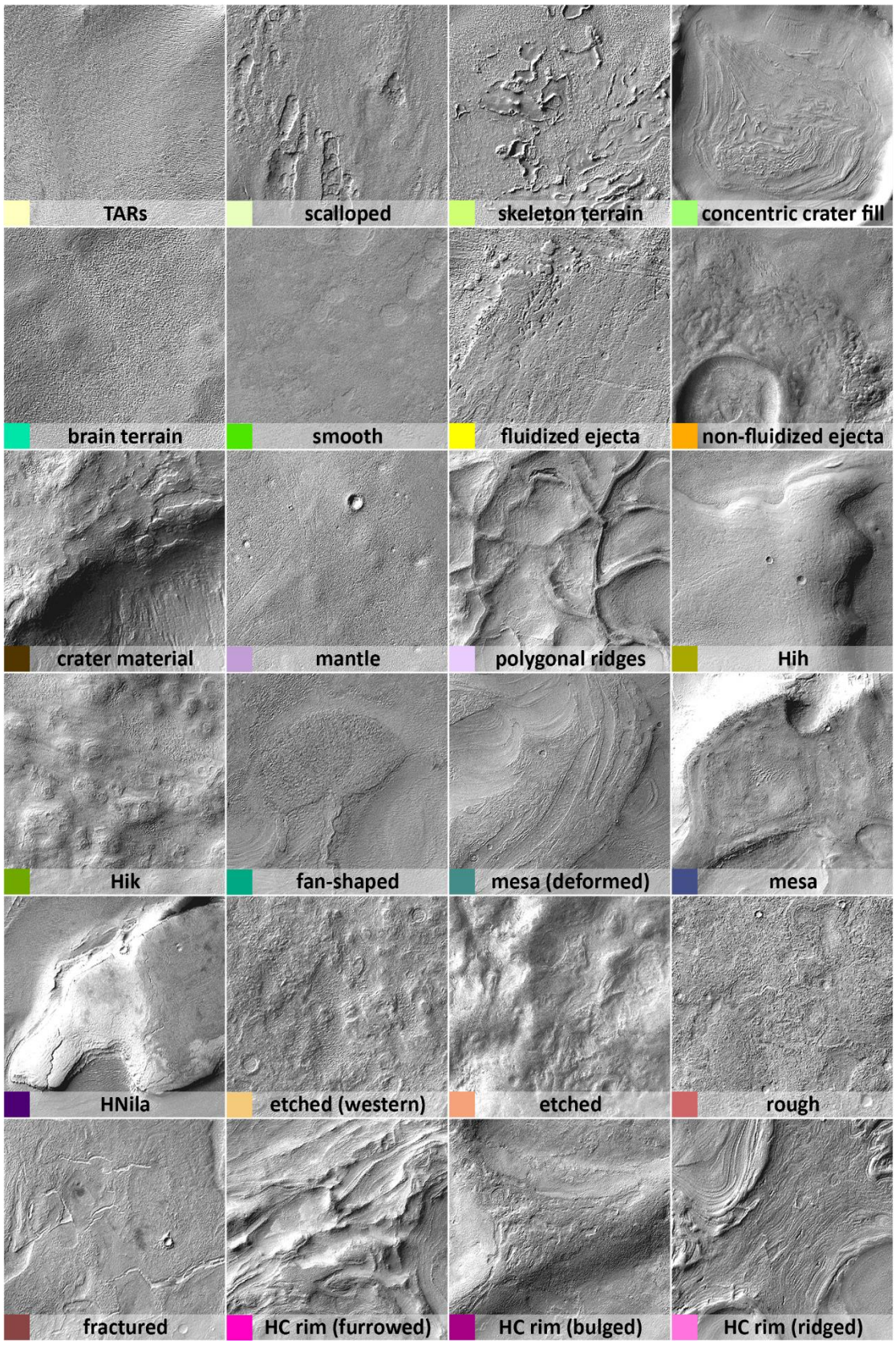

Figure 8: 5 x 5 km crops of our purpose-built CTX mosaic centered on the type localities of all

mapped morphologic units as listed in table 1.

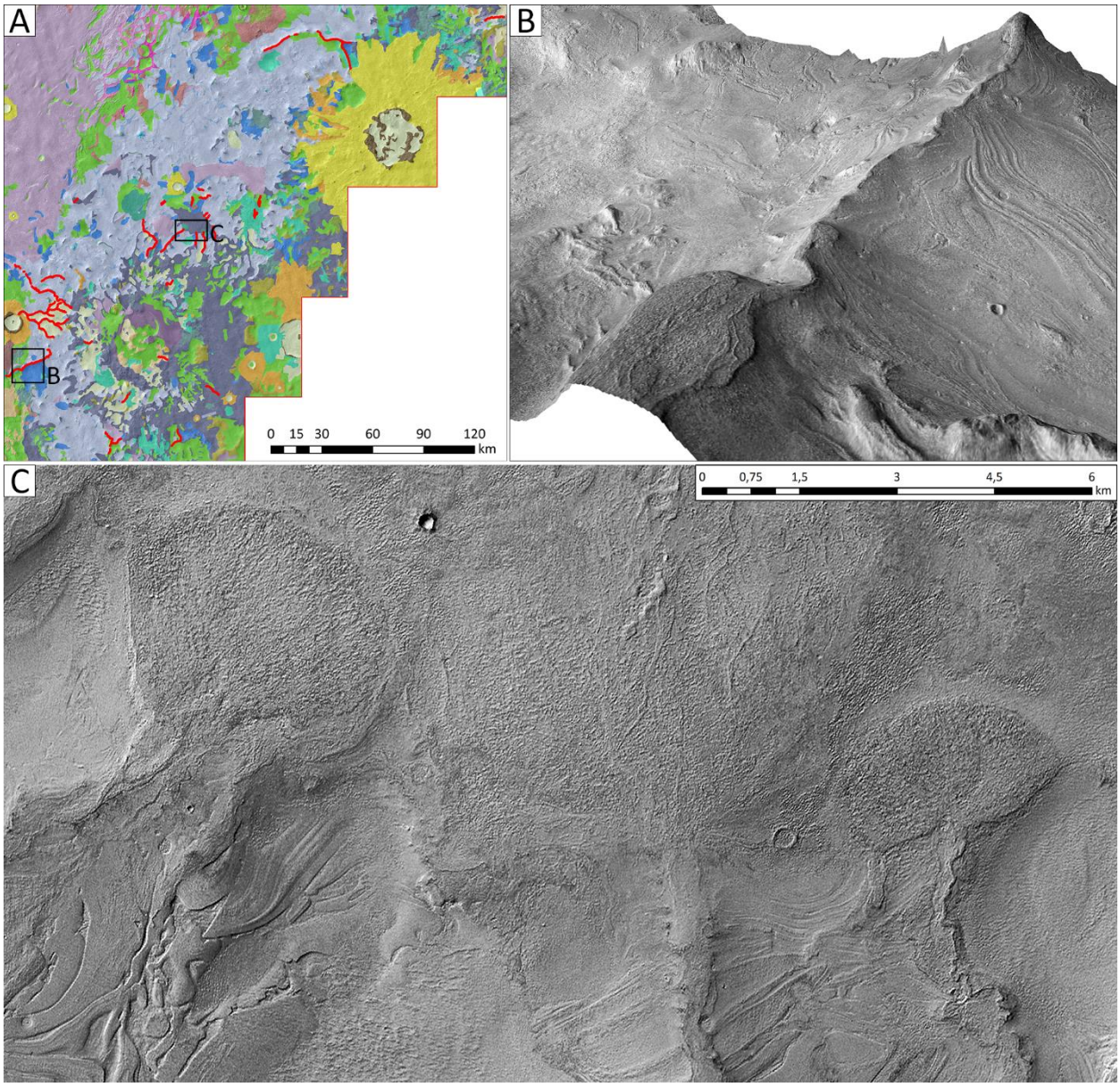

Figure 9: Observations of sinuous ridges surrounding the nameless "degraded crater" on western Hellas Planitia. A) Southeastern portion of our morphologic map (Fig. 2), showing Beloha crater in the upper right and the "degraded crater" in the lower left. Red lines mark sinuous ridges; black boxes indicate locations of (B) and (C). B) CTX image D20_034905_1382 projected onto a CTX stereo-DTM created in combination with image F21_044083_1382. The scene shows a prominent sinuous ridge terminating at an elevated plain characterized by a braiding system of smaller ridges (lower left). The ridge is located on top of a broader rise and the banded terrain can be seen

extending up on its flanks. C) Crop of our CTX mosaic showing the termini of three sinuous ridges, two of which transition into fan-shaped landforms that, in turn, are superposed on a *mesa* characterized by small, braiding ridges.

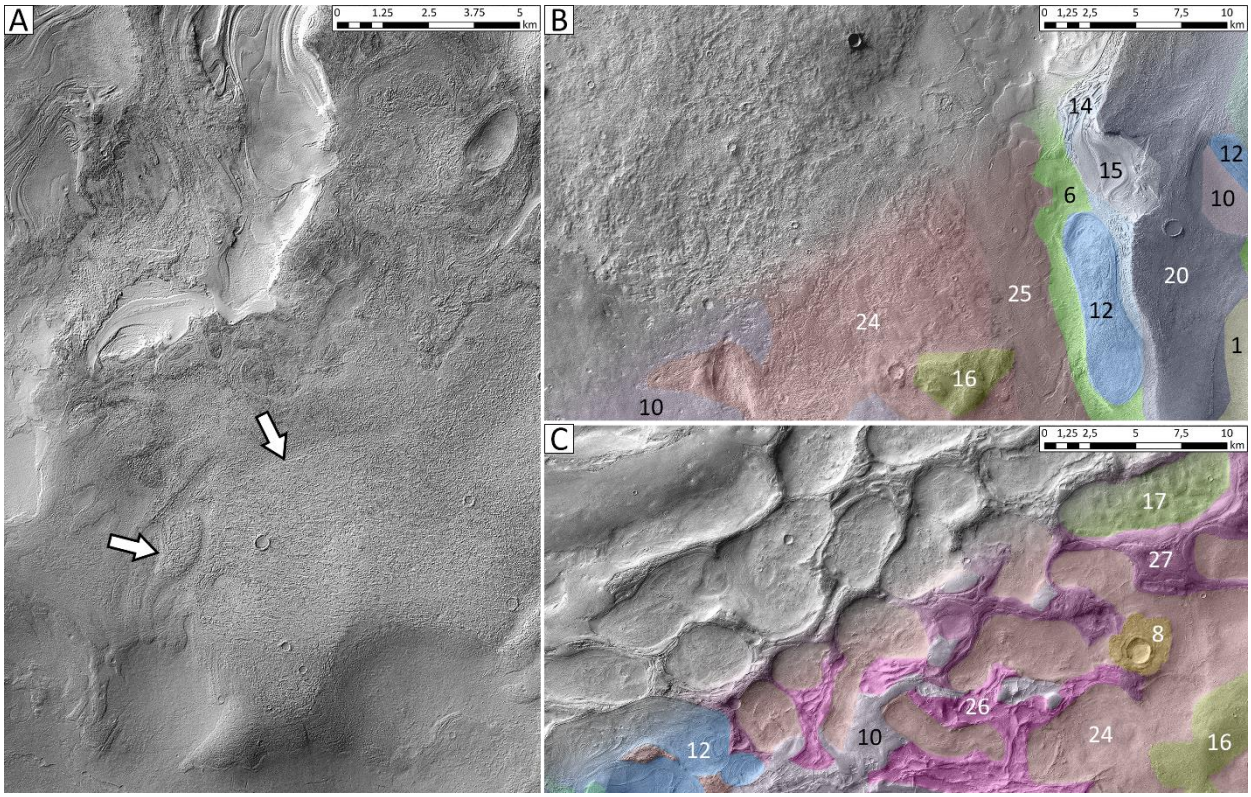

Figure 10: Stratigraphic observations pertaining to our morphologic map; image locations marked in Fig. 1B; all unit labels and numbers listed in Fig. 2B and table 1. A) Crop of our CTX mosaic showing unit *Hih* superposing a mesa (white arrows). B) CTX mosaic crop (lower right superposed by our morphologic map) showing from left to right: *Mantle (10)* superposing *rough (24)* material, which is also superposed by a zeugenberg of *Hih (16)*. *Rough* and *Hih* superpose *fractured (25)* material, which is also superposed by *smooth (6)* material, which in turn is overlain by banded terrain embaying a *mesa*. The latter is also partially covered by *TARs (1)*, *mantle*, and banded terrain. C) CTX mosaic crop (lower right superposed by our morphologic map) showing honeycomb cells being filled by banded terrain, *rough*, and *Hik (17)*. The scene also shows the transition from predominantly furrowed honeycomb rims (lower left) to predominantly bulged rims (upper right).

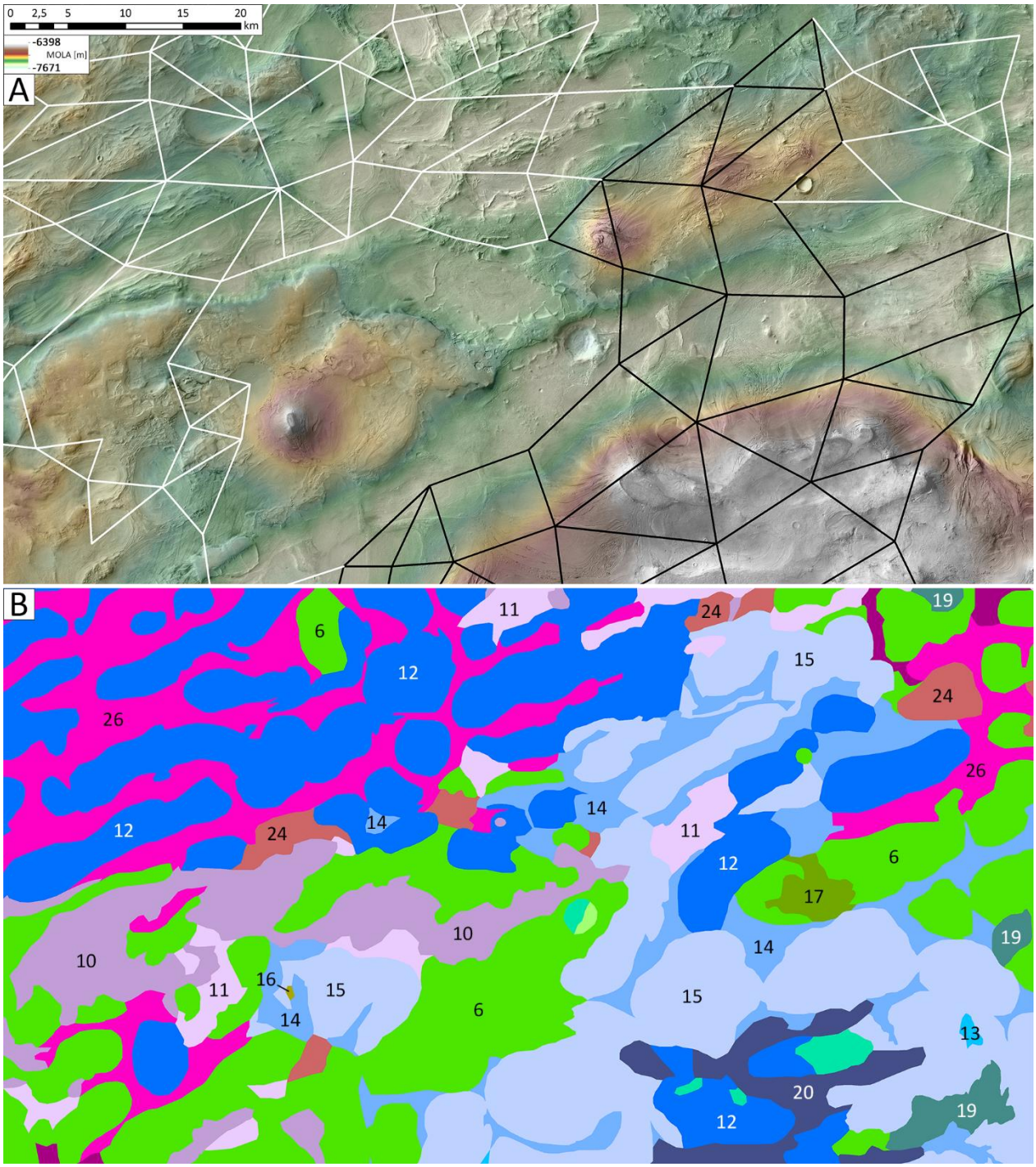

Figure 11: A) MOLA DTM superposing crop of our CTX mosaic; location shown in Fig. 1B; north is up. The scene is centered on the southern edge of the honeycomb terrain; a portion of the elevated interior formation can be seen in the lower right. The white lines connect the centers of adjacent honeycombs (here defined as kidney/cell-like depression confined by unit *HC rim*). The black lines

connect adjacent kidney/cell-shaped arrangements of convoluted banded terrain, i.e., *BT (convoluted)*, or by *mesas*. B) Portion of our morphologic map showing the same scene. Numbered units are listed in Fig. 2B and table 1.

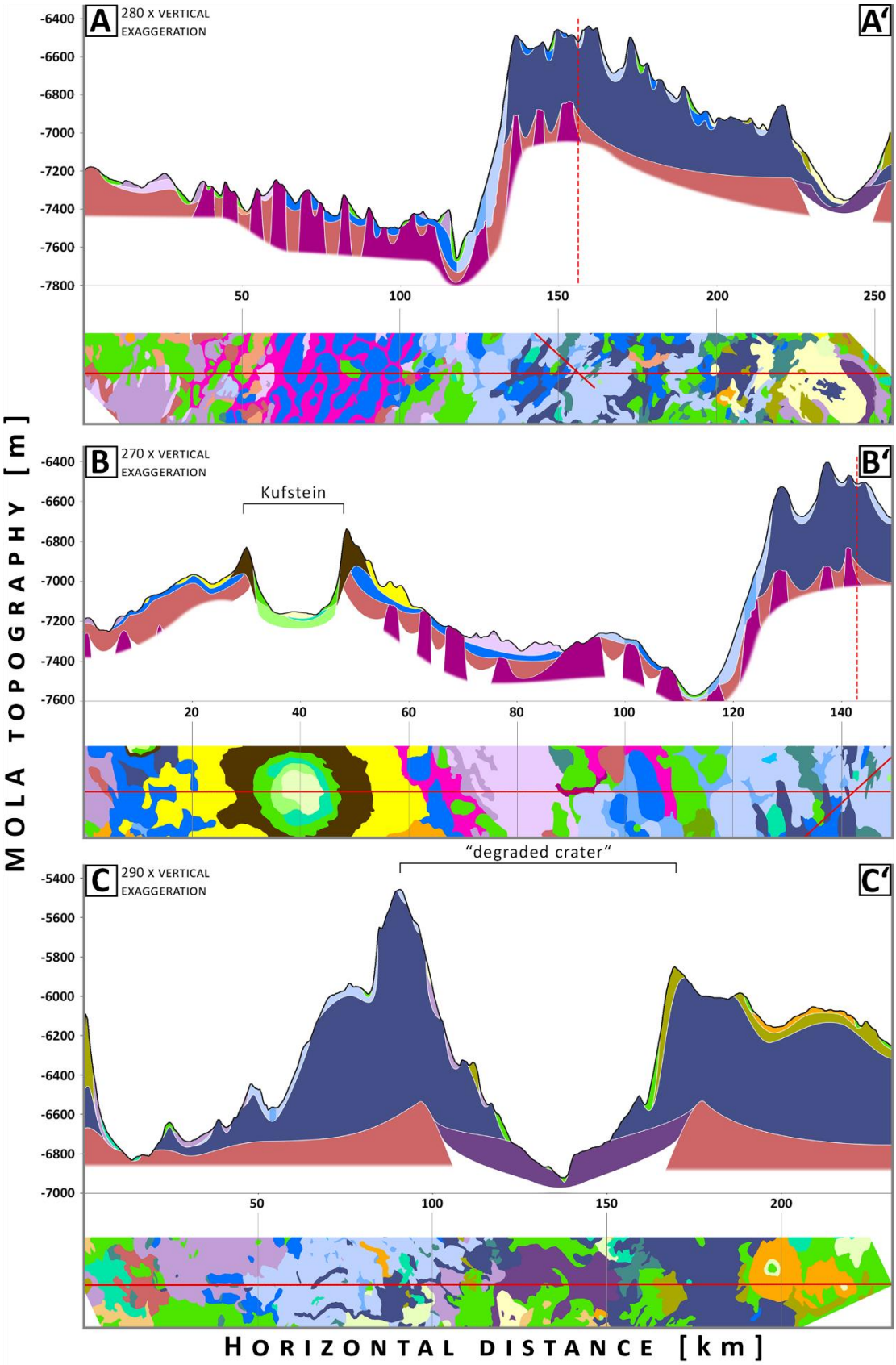
A
280 x VERTICAL EXAGGERATION
A'
-6400
-6600
-6800
-7000
-7200
-7400
-7600
-7800
50
100
150
200
250
B
270 x VERTICAL EXAGGERATION
B'
Kufstein
-6400
-6600
-6800
-7000
-7200
-7400
-7600
20
40
60
80
100
120
140
"degraded crater"
C
290 x VERTICAL EXAGGERATION
C'
-5400
-5600
-5800
-6000
-6200
-6400
-6600
-6800
-7000
50
100
150
200
MOLA TOPOGRAPHY [m]
HORIZONTAL DISTANCE [km]

Figure 12: A-C) Cross-sections illustrating our stratigraphic model along three traverses through our morphologic map as shown in Fig. 1B. The model is partially based on that by *Bernhardt et al. (2016a,b)* and was expanded as well as refined based on our observations outlined in section 5 and showcased in Fig. 10 und 11. The red dashed lines in (A) and (B) indicate the intersection of both profiles.

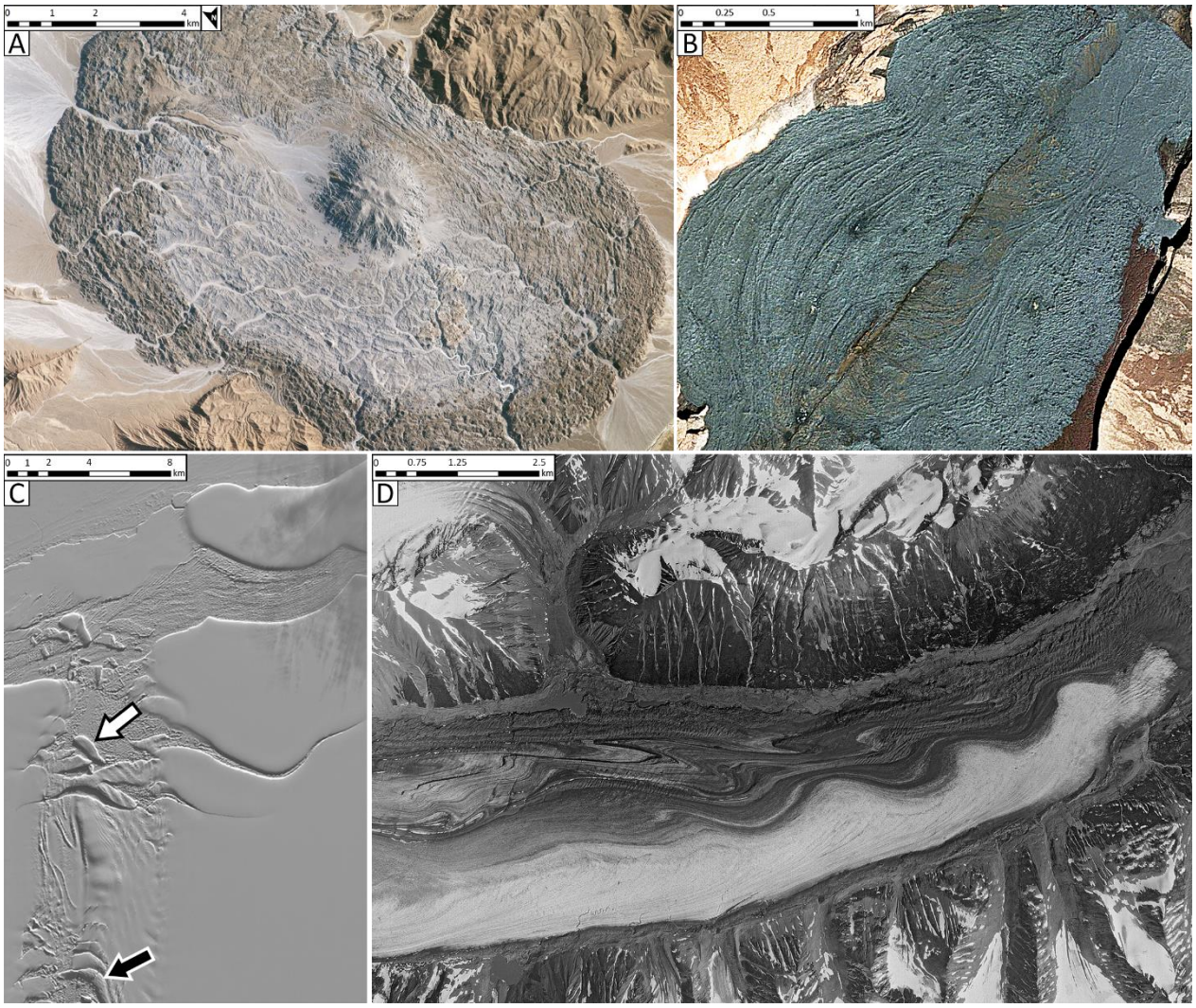

Figure 13: Terrestrial landforms investigated as potential analogs to the banded terrain. North is up in (B), (C), and (D). A) ISS astronaut photo ISS052-E-8401, acquired on 24 June 2017, of a salt dome surrounded by a salt glacier in the Zagros Mountains, southeastern Iran. B) QuickBird image, acquired 27 December 2002, of Mokuaweoweo, the central caldera of Mauna Loa, Hawai'i. It shows curvilinear ridges formed as flow lobes during the 1984 eruption of the fissure diagonally crossing the image. C) Landsat 8 image LC08_L1GT_191116 of the northern margin of the Ronne ice shelf at 48,73°W and 77,76°S, close to Berkner island. Interactions of stress fields create curvilinear compressional, and extensional, features. The white arrow points to a broken off, rotated slab; the black arrow show an area of upthrusting/buckling. D) USAF aerial photo acquired

on 22 June 1973 of Dusty Glacier in Kluane National Park, Yukon, Canada. Recurrent surges by a tributary glacier to the north create a curvilinear surface pattern.

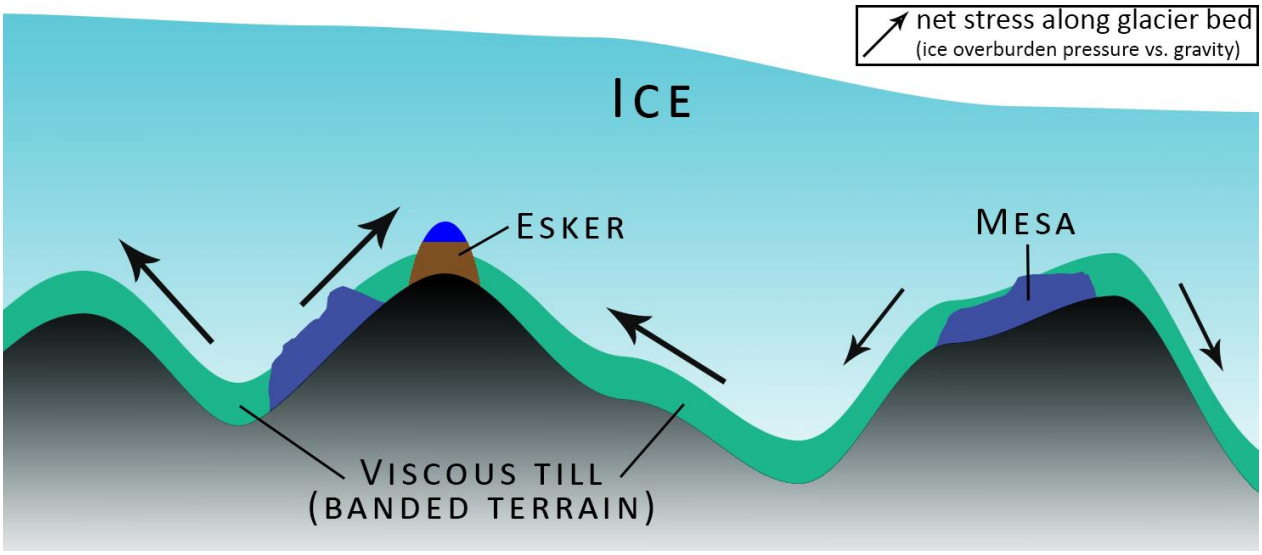

Figure 14: Illustration of our subglacial formation model for the banded terrain (see section 6.4).